The Astronomical Journal, 155:100 (20pp), 2018 February https://doi.org/10.3847/1538-3881/aaa5af

KELT-21b: A Hot Jupiter Transiting the Rapidly Rotating Metal-poor Late-A Primary of a Likely Hierarchical Triple System

Marshall C. Johnson[1], Joseph E. Rodriguez[2], George Zhou[2,43], Erica J. Gonzales[3,44], Phillip A. Cargile[2], Justin R. Crepp[4], Kaloyan Penev[5], Keivan G. Stassun[6], B. Scott Gaudi[1], Knicole D. Colón[7], Daniel J. Stevens[1], Klaus G. Strassmeier[8], Ilya Ilyin[8], Karen A. Collins[2], John F. Kielkopf[9], Thomas E. Oberst[10], Luke Maritch[11], Phillip A. Reed[11], Joao Gregorio[12], Valerio Bozza[13,14], Sebastiano Calchi Novati[13,15], Giuseppe D'Ago[16], Gaetano Scarpetta[13,17], Roberto Zambelli[18], David W. Latham[2], Allyson Bieryla[2], William D. Cochran[19], Michael Endl[19], Jamie Tayar[1], Aldo Serenelli[20,21], Victor Silva Aguirre[22], Seth P. Clarke[23], Maria Martinez[23,24], Michelle Spencer[23], Jason Trump[23], Michael D. Joner[23], Adam G. Bugg[23], Eric G. Hintz[23], Denise C. Stephens[23], Anicia Arredondo[25,26], Anissa Benzaid[25,27], Sormeh Yazdi[25,28], Kim K. McLeod[25], Eric L. N. Jensen[29], Daniel A. Hancock[30], Rebecca L. Sorber[30], David H. Kasper[30], Hannah Jang-Condell[30], Thomas G. Beatty[31,32], Thorsten Carroll[8], Jason Eastman[2], David James[2], Rudolf B. Kuhn[33,34], Jonathan Labadie-Bartz[35], Michael B. Lund[6], Matthias Mallonn[8], Joshua Pepper[35], Robert J. Siverd[36], Xinyu Yao[35], David H. Cohen[29], Ivan A. Curtis[37], D. L. DePoy[38,39], Benjamin J. Fulton[40,45], Matthew T. Penny[1], Howard Relles[2], Christopher Stockdale[41], Thiam-Guan Tan[42], and Steven Villanueva, Jr.[1,44]

[1] Department of Astronomy, The Ohio State University, 140 West 18th Ave., Columbus, OH 43210, USA; johnson.7240@osu.edu
[2] Harvard-Smithsonian Center for Astrophysics, 60 Garden St., Cambridge, MA 02138, USA
[3] Department of Astronomy and Astrophysics, University of California, Santa Cruz, 1156 High St., Santa Cruz, CA 95064, USA
[4] Department of Physics, University of Notre Dame, 225 Nieuwland Science Hall, Notre Dame, IN 46556, USA
[5] Department of Physics, University of Texas at Dallas, Richardson, TX 75080, USA
[6] Department of Physics and Astronomy, Vanderbilt University, Nashville, TN 37235, USA
[7] NASA Goddard Space Flight Center, Greenbelt, MD 20771, USA
[8] Leibniz-Institut für Astrophysik Potsdam (AIP), An der Sternwarte 16, D-14482 Potsdam, Germany
[9] Department of Physics and Astronomy, University of Louisville, Louisville, KY 40292, USA
[10] Department of Physics, Westminster College, New Wilmington, PA 16172, USA
[11] Department of Physical Sciences, Kutztown University, Kutztown, PA 19530, USA
[12] Atalaia Group & CROW Observatory, Portalegre, Portugal
[13] Dipartimento di Fisica "E.R. Caianiello", Università di Salerno, Via Giovanni Paolo II 132, I-84084 Fisciano (SA), Italy
[14] Istituto Nazionale di Fisica Nucleare, Sezione di Napoli, I-80126 Napoli, Italy
[15] IPAC, Mail Code 100-22, California Institute of Technology, 1200 East California Boulevard, Pasadena, CA 91125, USA
[16] INAF-Osservatorio Astronomico di Capodimonte, Salita Moiariello 16, I-80131, Napoli, Italy
[17] Instituto Internazionale per gli Alti Studi Scientifici (IIASS), Via G. Pellegrino 19, I-84019 Vietri sul Mare (SA), Italy
[18] Società Astronomica Lunae, Castelnuovo Magra I-19030, Italy
[19] McDonald Observatory, University of Texas at Austin, 2515 Speedway, Stop C1400, Austin, TX 78712, USA
[20] Institute of Space Sciences (*ICE*, CSIC), Campus UAB, Carrer de Can Magrans S/N, E-08193, Barcelona, Spain
[21] Institut d'Estudis Espacials de Catalunya (IEEC), Edifici Nexus, C/Gran Capita, 2-4, E-08034, Barcelona, Spain
[22] Stellar Astrophysics Centre, Department of Physics and Astronomy, Aarhus University, Ny Munkegade 120, DK-8000 Aarhus C, Denmark
[23] Department of Physics and Astronomy, Brigham Young University, Provo, UT 84602, USA
[24] University of California, Merced, Merced, CA 95343 USA
[25] Department of Astronomy, Wellesley College, Wellesley, MA 02481, USA
[26] University of Central Florida, Orlando, FL 32816 USA
[27] Boston University, Boston, MA 02215, USA
[28] Massachusetts Institute of Technology, Cambridge, MA 02139, USA
[29] Department of Physics and Astronomy, Swarthmore College, Swarthmore, PA 19081, USA
[30] Department of Physics and Astronomy, University of Wyoming, Laramie, WY 82071, USA
[31] Department of Astronomy & Astrophysics, The Pennsylvania State University, 525 Davey Lab, University Park, PA 16802, USA
[32] Center for Exoplanets and Habitable Worlds, The Pennsylvania State University, 525 Davey Lab, University Park, PA 16802, USA
[33] South African Astronomical Observatory, P.O. Box 9, Observatory, 7935 Cape Town, South Africa
[34] Southern African Large Telescope, P.O. Box 9, Observatory, 7935 Cape Town, South Africa
[35] Department of Physics, Lehigh University, 16 Memorial Drive East, Bethlehem, PA 18015, USA
[36] Las Cumbres Observatory, 6740 Cortona Dr., Ste 102, Goleta, CA 93117, USA
[37] ICO, Adelaide, South Australia, Australia
[38] George P. and Cynthia Woods Mitchell Institute for Fundamental Physics and Astronomy, Texas A&M University, College Station, TX 77843, USA
[39] Department of Physics and Astronomy, Texas A&M University, College Station, TX 77843, USA
[40] California Institute of Technology, Pasadena, CA 91125, USA
[41] Hazelwood Observatory, Churchill, Victoria, Australia
[42] Perth Exoplanet Survey Telescope, Perth, Australia
Received 2017 December 7; accepted 2017 December 20; published 2018 February 1

Abstract

We present the discovery of KELT-21b, a hot Jupiter transiting the $V = 10.5$ A8V star HD 332124. The planet has an orbital period of $P = 3.6127647 \pm 0.0000033$ days and a radius of $1.586^{+0.039}_{-0.040}$ R_J. We set an upper limit on the

[43] Hubble Fellow.
[44] NSF Graduate Fellow.
[45] Texaco Fellow.

planetary mass of $M_P < 3.91\ M_J$ at 3σ confidence. We confirmed the planetary nature of the transiting companion using this mass limit and Doppler tomographic observations to verify that the companion transits HD 332124. These data also demonstrate that the planetary orbit is well-aligned with the stellar spin, with a sky-projected spin–orbit misalignment of $\lambda = -5.6^{+1.7}_{-1.9}°$. The star has $T_{\rm eff} = 7598^{+81}_{-84}$ K, $M_* = 1.458^{+0.029}_{-0.028}\ M_\odot$, $R_* = 1.638 \pm 0.034\ R_\odot$, and $v \sin I_* = 146$ km s^{-1}, the highest projected rotation velocity of any star known to host a transiting hot Jupiter. The star also appears to be somewhat metal poor and α-enhanced, with [Fe/H] $= -0.405^{+0.032}_{-0.033}$ and [α/Fe] $= 0.145 \pm 0.053$; these abundances are unusual, but not extraordinary, for a young star with thin-disk kinematics like KELT-21. High-resolution imaging observations revealed the presence of a pair of stellar companions to KELT-21, located at a separation of $1\farcs2$ and with a combined contrast of $\Delta K_S = 6.39 \pm 0.06$ with respect to the primary. Although these companions are most likely physically associated with KELT-21, we cannot confirm this with our current data. If associated, the candidate companions KELT-21 B and C would each have masses of $\sim$0.12 $M_\odot$, a projected mutual separation of $\sim$20 au, and a projected separation of $\sim$500 au from KELT-21. KELT-21b may be one of only a handful of known transiting planets in hierarchical triple stellar systems.

Key words: planets and satellites: detection – planets and satellites: gaseous planets – methods: observational – stars: individual (HD 332124) – techniques: photometric – techniques: radial velocities

Supporting material: data behind figures

1. Introduction

Most of the currently known exoplanets orbit relatively cool, low-mass (FGKM) stars, with $T_{\rm eff} < 6500$ K. The reason for this is likely observational bias rather than an actual paucity of planets around hotter stars: traditionally, precise radial velocity (RV) observations have been the dominant method to find exoplanets, and, more recently, confirm transiting giant planets. Hot stars, however, typically rotate rapidly. Above the Kraft break (Kraft 1967), at $T_{\rm eff} \sim 6250$ K, stars no longer have the thick surface convective zones necessary to maintain a strong magnetic dynamo which can efficiently transport angular momentum to the outgoing stellar wind. More massive stars therefore tend to retain their initial rapid rotation throughout their main-sequence lifetimes. Typical $v \sin I_*$ values are in excess of 100 km s^{-1} for the entire B9–F2 spectral type range (Royer et al. 2007). The rotational broadening of these stars' lines and the paucity of absorption lines from their hot atmospheres make it difficult or impossible to measure the stellar reflex motion due to even giant planets. For this reason, stars hotter than mid-F have typically been ignored by planet surveys. Planets around these stars were too difficult to find with RVs or confirm as transiting planets, and massive stars are too rare to cause a significant number of microlensing events.

There are, however, other ways to discover planets around early-type stars. Direct imaging observations are largely insensitive to stellar properties. Indeed, early-type stars are *more* amenable to direct imaging observations than are solar-type stars because they are on average younger and their planets therefore hotter and brighter. Many of the known directly imaged planets are around such stars (e.g., Marois et al. 2008, 2010; Lagrange et al. 2010).

Planets can also be found around these stars by observing them after they have left the main sequence. As they evolve, the stars cool and expand, slowing their rotation and increasing the number of spectral lines, thus becoming amenable to precise RV observations. RV surveys have discovered a large number of giant planets around intermediate-mass subgiant and giant stars (e.g., Johnson et al. 2011; Reffert et al. 2015), which suggest that the frequency of giant planets around A stars may be higher than that around FGK stars. The issue of whether these "retired A stars" are actually intermediate-mass stars or, rather, lower-mass interlopers, is, however, controversial (e.g., Lloyd 2011; Johnson et al. 2013; Schlaufman & Winn 2013; Stello et al. 2017).

Despite the success of direct imaging and RV surveys, there are still limitations to these methods as far as probing the overall planetary populations of A and early F stars. Principally, neither method can probe the close-in, short-period population of planets, similar to those that *Kepler* has discovered around lower-mass stars. The angular separations between these planets and their host stars are much too small to be resolved with current or future direct imaging facilities, and such short-period planets will have been engulfed and destroyed as the stellar radii expand during the evolution off of the main sequence.

Although early-type stars have typically been ignored by transit surveys, efforts to discover planets around these stars have been increasingly successful. The first transiting planet to be discovered around a hot, rapidly rotating star was WASP-33b (Collier Cameron et al. 2010). It was confirmed using a combination of Doppler tomography (where the perturbation to the rotationally broadened stellar line profile during the transit due to the Rossiter–McLaughlin effect is spectroscopically resolved, showing that the planet candidate orbits the target star and is not a background eclipsing binary) and low-precision RV observations (showing that the transiting object has a mass below the substellar limit). Since then, a growing number of transiting hot Jupiters around rapidly rotating A and early F stars have been discovered and (in most cases) confirmed using Doppler tomography, such as CoRoT-11b (Gandolfi et al. 2010, 2012), Kepler-13Ab (Szabó et al. 2011; Johnson et al. 2014), HAT-P-57b (Hartman et al. 2015), MASCARA-1b (Talens et al. 2017a), and XO-6b (Crouzet et al. 2017).

The Kilodegree Extremely Little Telescope (KELT; Pepper et al. 2003, 2007, 2012) project has been particularly effective in finding hot Jupiters around A and early F stars. Indeed, more than half of the KELT planets discovered to date orbit stars above the Kraft break (Siverd et al. 2012; Pepper et al. 2013; Collins et al. 2014; Bieryla et al. 2015; Zhou et al. 2016b; Gaudi et al. 2017; Lund et al. 2017; McLeod et al. 2017; Siverd et al. 2018; Stevens et al. 2017; Temple et al. 2017), or, in the case of KELT-11, was above the Kraft break when it was on the main sequence (Pepper et al. 2017). As discussed in Lund et al. (2017), this is partially by design and Malmquist bias, and partially by accident. As KELT was designed to target brighter

stars ($8 < V < 11$) than those in other transit surveys, hot, bright stars are overrepresented in its sample due to the larger volume probed. Additionally, many of the transiting hot Jupiters around cooler stars in this magnitude range had already been discovered by the time KELT obtained a sufficient quantity of data to find planets. Together, these two forces drove us toward the discovery of planets around hot stars.

Another region of parameter space that has not been fully explored is hot Jupiter occurrence as a function of stellar multiplicity. Although there are a large number of known hot Jupiters in binary stellar systems—indeed, Ngo et al. (2016) found a higher occurrence rate of stellar binary companions for hot Jupiter hosts than that for field stars—only a handful of hot Jupiters are known in higher-order stellar systems. Four transiting hot Jupiters are known in hierarchical triple systems, KELT-4 (Eastman et al. 2016), HAT-P-8, WASP-12 (Bechter et al. 2014), and Kepler-13 (Santerne et al. 2012), and none in higher-order multiples. In the first three of these, the hot Jupiter orbits the primary star, the mass ratios between the primary and secondary/tertiary stars are large, and the companions were resolved with direct imaging. In Kepler-13, the primary and secondary stars are of a similar mass while the tertiary star is much less massive, and the tertiary was discovered through RV observations of the secondary (Santerne et al. 2012; Johnson et al. 2014). Transit survey follow-up is typically biased against the latter type of system; visual binaries are often excluded from survey target lists, and the presence of multiple lines in a spectrum (especially if some of them are moving) is typically taken as reason to conclude that a planet candidate is a false positive, even if such a system could in fact host a planet (see Siverd et al. 2018 for a recent case of a confirmed planet discovered in a binary stellar system with two sets of lines in the spectra). Planets in hierarchical triple systems are also of interest because their dynamics are richer than those of hot Jupiters in stellar binaries (e.g., Fang et al. 2017; Hamers 2017); certain configurations could enhance the efficiency of hot Jupiter formation by high-eccentricity (Kozai–Lidov) migration (Hamers 2017). Such extreme systems help us test the limits of planet formation and migration.

Here, we present the discovery of a new transiting hot Jupiter, KELT-21b, confirmed using Doppler tomography. KELT-21 is not only the most rapidly rotating star known to host a transiting giant planet (with $v \sin I_* = 146$ km s^{-1}) but also is likely one of the few planet-host stars known to be part of a hierarchical triple system.

2. Discovery and Follow-up Observations

2.1. Discovery

The star HD 332124 was observed by the KELT-North telescope in KELT-North Field 11 (KN11; center coordinates R.A.=19^{h}27^{m}00^s.0, decl. = +31°39′56.″2 J2000.0). This is the same field that also yielded our other two most rapidly rotating planet hosts, KELT-9b (Gaudi et al. 2017) and KELT-20b/MASCARA-2b (Lund et al. 2017; Talens et al. 2017b), as well as KELT-8b (Fulton et al. 2015). In the analysis of 6783 observations of HD 332124 obtained between 2007 May 29 and 2014 November 25 UT, we identified a candidate transit signal with a period of 3.612782 days and a depth of ~1%; the target was given the KELT candidate ID of KC11C039077. Our data reduction and analysis and candidate selection procedures are described in Siverd et al. (2012). We show the KELT photometry of KELT-21 in Figure 1 and list the literature parameters of the system in Table 1.

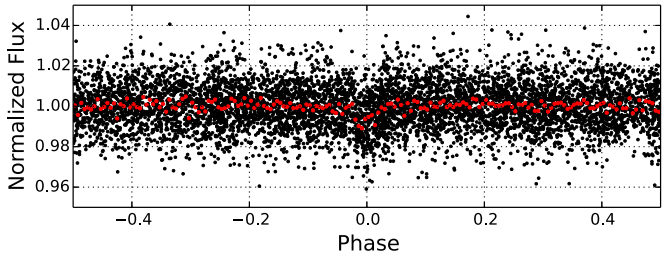

Figure 1. Discovery light curve for KELT-21b based on 6783 observations from the KELT-North telescope. The data have been phase-folded on the preliminary value for the period, 3.612782 days. The black points depict the data, while the red points are the data binned on a five-minute timescale. The data used to create this figure are available.

Table 1
System Properties of KELT-21

Other Identifiers	HD 332124		
	TYC 2676-1274-1		
	2MASS J20191200+3234517		
	TIC 203189770		
Parameter	Description	Value	Reference
α_{J2000}	Right ascension (R.A.)	20^{h}19^{m}12^s.004	1
δ_{J2000}	Declination (decl)	+32°34′51.″77	1
B_T	Tycho B_T mag.	10.76 ± 0.04	1
V_T	Tycho V_T mag.	10.48 ± 0.04	1
J	2MASS J mag.	10.149 ± 0.022	2
H	2MASS H mag.	10.121 ± 0.021	2
K_S	2MASS K_S mag.	10.090 ± 0.014	2
W1	*WISE1* magnitude	10.064 ± 0.022	3
W2	*WISE2* magnitude	10.106 ± 0.021	3
W3	*WISE3* magnitude	10.252 ± 0.069	3
W4	*WISE4* magnitude	>9.158	3
μ_α	*Gaia* DR1 proper motion in R.A. (mas yr^{-1})	1.933 ± 0.791	4
μ_δ	*Gaia* DR1 proper motion in DEC (mas yr^{-1})	−1.317 ± 0.804	4
RV[a]	Systemic radial velocity (km s^{-1})	−13.0 ± 1.0	Section 2.3
$v \sin I_*$	Stellar rotational velocity (km s^{-1})	146.03 ± 0.48	Section 4.2
Spec. Type	Spectral Type	A8V	Section 4.2
Age	Age (Gyr)	1.6 ± 0.1	Section 3.3
d	Distance (pc)	415 ± 49	4
Π	Parallax (mas)	2.41 ± 0.28	4
A_V	Visual extinction (mag)	$0.00^{+0.34}_{-0.00}$	Section 3.1
U[b]	Space motion (km s^{-1})	9.2 ± 1.9	Section 3.4
V	Space motion (km s^{-1})	−0.5 ± 1.1	Section 3.4
W	Space motion (km s^{-1})	8.9 ± 1.9	Section 3.4

Notes.
[a] *RV* is defined on the IAU system.
[b] *U* is positive in the direction of the Galactic Center.

References. 1. Høg et al. (2000), 2. Cutri et al. (2003), 3. Cutri et al. (2014), 4. *Gaia* Collaboration et al. (2016) *Gaia* DR1 (http://gea.esac.esa.int/archive/), corrected for the position-dependent systematic offset found by Stassun & Torres (2016).

Table 2
Photometric Follow-up Observations of KELT-21b

Observatory	Location	Aperture (m)	Plate scale ($''$ pix^{-1})	Date (UT)	Filter	Exposure Time (s)	Detrending Parameters[a]
SUO	Fisciano Salerno, Italy	0.3556	0.59	2014 Aug 28	I	60	Airmass
ZRO	Sarzana, Italy	0.3048	0.92	2014 Oct 25	V	200	Airmass
CROW	Portalegre, Portugal	0.3048	0.82	2016 Jul 18	V	120	Airmass, Meridian flip
KUO	PA, USA	0.6096	0.76	2016 Aug 24	V	60	Airmass
KUO	PA, USA	0.6096	0.76	2016 Aug 24	I	60	Airmass
WCO	PA, USA	0.35	1.44	2016 Aug 24	r'	15	Airmass
ULMT	AZ, USA	0.6096	0.39	2017 May 29	g'	50	Airmass
ULMT	AZ, USA	0.6096	0.39	2017 May 29	i'	100	Airmass

Note.
[a] Photometric parameters allowed to vary in global fits and described in the text. Abbreviations: SUO: Salerno University Observatory; ZRO: Zambelli's Robotic Observatory; CROW: Canela's Robotic Observatory; KUO: Kutztown Observatory, Kutztown University; WCO: Westminster College Observatory; ULMT: University of Louisville Manner Telescope.

2.2. Photometric Follow-up from KELT-FUN

After identification of the candidate transit signal in the KELT-North photometry, we obtained follow-up transit photometry of this target using the KELT Follow-Up Network (KFUN; K. A. Collins et al. 2018, in preparation). The purpose of these observations was to first confirm the existence of a transit event for this star, and then check that the transit shape was consistent with that of a planet and that the transit was achromatic. We describe the facilities and observations obtained briefly in the following sections; KELT-21 passed all of these tests, and so we then pursued spectroscopic observations to confirm the planetary nature of the candidate (Section 2.3). We scheduled observations using a modified version of the TAPIR observation planning software (Jensen 2013), and all observations were reduced using the AstroImageJ package[46] (Collins & Kielkopf 2013; Collins et al. 2017).

We observed portions of seven transits of KELT-21b between 2014 August 7 and 2017 May 29 UT; two of these were observed simultaneously in two different filters, for a total of nine transit light curves. Details of these are listed in Table 2, and the data are shown in Figure 2.

2.2.1. Salerno University Observatory

We observed the transit of 2014 August 28 at the Salerno University Observatory, located in Fisciano, Italy. At the time of the observations, it hosted a Celestron C14 telescope (0.35 m aperture) on a German equatorial mount, with an SBIG ST2000XM CCD and standard Bessell filters; the observations were conducted in the I band. The field of view was $11' \times 14'$ with a plate scale of $0\farcs59$ pix^{-1}.

2.2.2. Roberto Zambelli's Observatory

We observed the ingress of the transit of 2014 October 25 at Zambelli's Robotic Observatory (ZRO) in Sarzana, Italy. We used a Meade 12″ (0.3048 m) $f/10$ telescope with a focal reducer, giving a final value of $f/6.3$. The images were captured using an SBIG ST8XME CCD. The CCD has 1530×1020 pixels and a $23\farcm52 \times 15\farcm68$ field of view, giving a plate scale of $0\farcs92$ pix^{-1}. The observations were obtained in the V band with an exposure length of 200 s. Strong winds halted the observations about an hour before mid-transit.

2.2.3. Canela's Robotic Observatory

We observed a transit of KELT-21b on 2016 July 18 from Canela's Robotic Observatory (CROW) in Portalegre, Portugal. Located at an altitude of 600 m, the observatory is equipped with a Meade SCT 30 cm telescope with $f/5.56$ and an SBIG ST-10XME CCD camera with a KAF3200ME detector, giving a plate scale of $0\farcs82$ pix^{-1}. We observed with a Johnson V filter manufactured by Custom Scientific.

2.2.4. Kutztown University Observatory

We observed KELT-21 from the Kutztown University Observatory (KUO) for seven consecutive hours on 2016 August 24 in alternating V and I filters, covering the full ∼4 hr transit of KELT-21b and an additional 3 hr of pre-ingress and post-egress baseline. A total of 332 images were collected (166 in each band) with exposure times of 60 s each. We used KUO's 0.6 m $f/8$ Ritchey–Chrétien optical telescope and an SBIG STXL-6303E CCD camera. The detector's array of 3072×2048 9 μm pixels provides a $19\farcm5 \times 13\farcm0$ field of view, and with 2×2 binning, the effective plate scale is $0\farcs76$ pix^{-1}. The CCD was kept at an operating temperature of −25° C. KUO is located on the campus of Kutztown University in Kutztown, Pennsylvania, USA.

2.2.5. Westminster College Observatory

We observed a full transit of KELT-21b from the Westminster College Observatory (WCO), Pennsylvania, USA, on 2016 August 24 UT in the r' filter. The observations employed a 0.35 m $f/11$ Celestron C14 Schmidt–Cassegrain telescope and an SBIG STL-6303E CCD camera with a ∼3k × 2k array of 9 μm pixels, yielding a $24' \times 16'$ field of view and $1\farcs44$ pix^{-1} plate scale at 3×3 pixel binning.

2.2.6. University of Louisville Manner Telescope

We observed a full transit of KELT-21b using the University of Louisville Manner Telescope (ULMT) located at the Mt. Lemmon summit of Steward Observatory, Arizona, USA, on 2017 May 29 UT. Exposures were taken in alternating g and i filters, yielding pseudo-simultaneous observations in the two bands. The observations employed a 0.6 m $f/8$ RC Optical

[46] http://www.astro.louisville.edu/software/astroimagej/

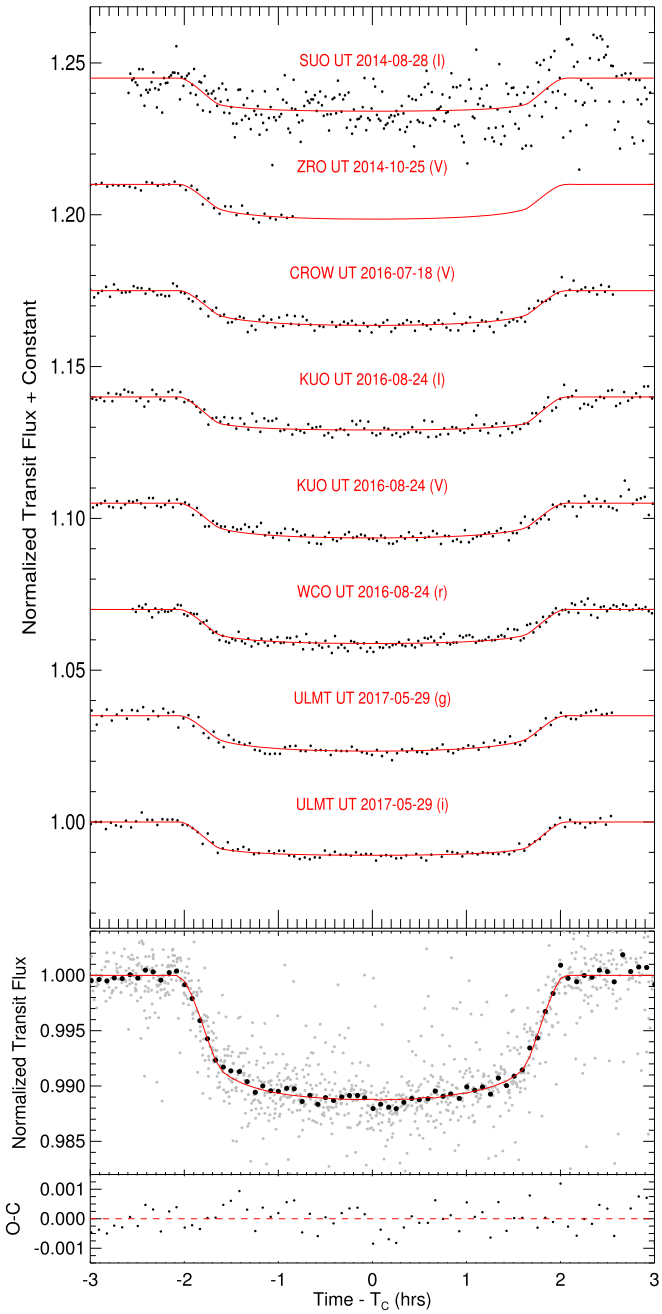

Figure 2. (Top) Transit light curves of KELT-21b from the KELT Follow-up Network. The red line represents the best-fit model from the global fit in that photometric band. Each light curve is offset vertically by an arbitrary amount for clarity. (Bottom) All follow-up transits combined into one light curve (gray) and a five-minute binned light curve (black). The red line is the combined and binned models for each transit. We emphasize that the combined light curve is only for display purposes; the individual transit light curves were used in our analysis. The data used to create this figure are available.

Systems Ritchey–Chrétien telescope and an SBIG STX-16803 CCD camera with a 4k × 4k array of 9 μm pixels, yielding a 26.′6 × 26.′6 field of view and 0.″39 pix^{-1} plate scale. These photometric observations were obtained simultaneously with the spectroscopic observations with the LBT/Potsdam Échelle Polarimetric and Spectroscopic Instrument (PEPSI) and Tillinghast Reflector Échelle Spectrograph (TRES) described below.

2.3. Spectroscopic Follow-up

As the photometric follow-up campaign confirmed the existence of transits for KELT-21 and showed that the transits were both achromatic and with a shape appropriate for a transiting planet, we began spectroscopic follow-up observations. These consisted of three steps: first, reconnaissance spectroscopy to measure the stellar parameters; second, low-precision RV observations to exclude large RV variations that would have indicated that the transiting object was an M dwarf or a brown dwarf; and, finally, Doppler tomographic observations to confirm that the transiting object transits the star KELT-21. In the following sections, we describe these observations.

2.3.1. TRES Spectra

We obtained 20 spectra of KELT-21 with TRES (e.g., Fűrész 2008) on the 1.5 m telescope at Fred Lawrence Whipple Observatory, Mt. Hopkins, Arizona, USA. TRES is a fiber-fed échelle spectrograph with a spectral coverage of 3900–9100 Å over 51 échelle orders, with a spectral resolving power of $R = 44{,}000$. The spectra are recorded by a 2048 × 4608 CCD. We obtained 11 of the observations to constrain the mass of the planet, over the full range of out-of-transit phases, although we excluded two of these which happened to be obtained in transit from the analysis. We also obtained nine spectra during the transit on 2017 May 29 UT to measure the Doppler tomographic signal of the transiting planet. These latter data are described further in Section 4.1. Most of the observations had an exposure time of 1800 s, but a few had lengths of as short as 240 s or as long as 3000 s. The best TRES spectra have a per-pixel signal-to-noise ratio of ∼65 near 5200 Å.

We reduced these data using version 2.55 of the TRES pipeline, a custom pipeline written in IDL by L. Buchhave. We analyzed the TRES spectra using two different methods, one in order to measure the absolute RV of KELT-21 and another in order to measure the relative RVs of the star to constrain the planetary mass.

In order to determine the absolute velocity of KELT-21, we used only the six strongest out-of-transit TRES spectra. We cross-correlated these with a rotating model template spectrum with parameters similar to that of KELT-21 (see Sections 3.2 and 4.2). The weighted average and standard deviation derived from these six spectra (following Buchhave et al. 2010; Quinn et al. 2012) is -12.4 ± 1.0 km s^{-1} on the TRES native system; converting to the IAU velocity system, this gives an absolute RV of -13.0 ± 1.0 km s^{-1} for KELT-21.

The relative RVs were obtained by fitting the line broadening profiles of each spectrum. The line broadening profiles are derived via a least-squares deconvolution approach, as per Donati et al. (1997), against a non-rotating synthetic template derived using the SPECTRUM[47] code with the ATLAS9 atmosphere models (Castelli & Kurucz 2004) over the wavelength range of 3900–6250 Å. The broadening kernel is fitted with a function accounting for rotation, macroturbulence, and instrumental broadening, and is shifted in velocity to match the observation. The uncertainties were determined from the order-to-order velocity scatter divided by the square root of the number of orders used.

[47] http://www.appstate.edu/~grayro/spectrum/spectrum.html

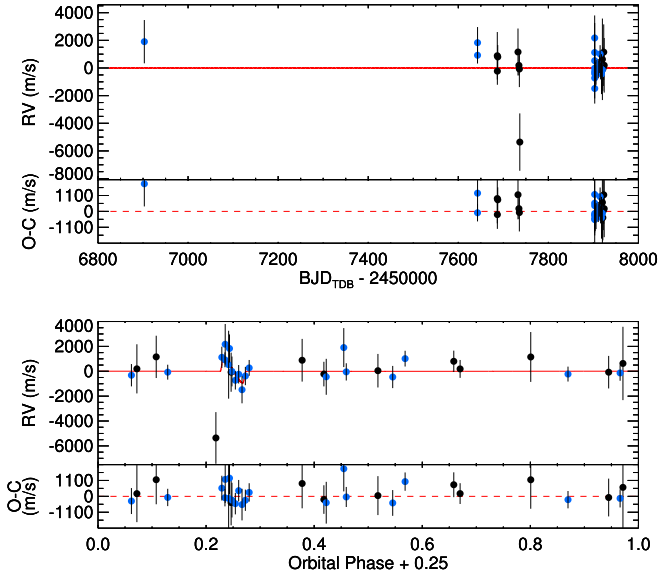

Figure 3. (Top) The TS23 (black) and TRES (blue) RV measurements of KELT-21 with the best-fit model shown in red. The systemic RV has been subtracted from each data set. The residuals to the fit are shown below. (Bottom) The RV measurements phase-folded to the global fit-determined ephemeris. The predicted RV Rossiter–McLaughlin signal is shown at 0.25 phase. The residuals are shown below.

We show these data in Figure 3 and list the RV measurements in Table 3.

2.3.2. TS23 Spectra

We obtained 12 spectra of KELT-21 covering a wide range of orbital phases using the 2.7 m Harlan J. Smith Telescope at McDonald Observatory, Texas, USA, and its Robert G. Tull Coudé Spectrograph (Tull et al. 1995). We conducted these observations between 2016 October 25 and 2017 June 19 UT. Observing conditions ranged from clear to thin or scattered clouds, with seeing typically between 1.″0 and 1.″5 but occasionally as poor as 2.″0.

We used the spectrograph in its TS23 configuration, with a 1.″2 × 8.″2 slit providing a resolving power of $R = 60{,}000$ and coverage from 3570 Å to 10200 Å; the spectral coverage is complete below 5691 Å. A 2048 × 2048 Tektronix CCD captures 58 spectral orders. Exposure times ranged from 120 to 1200 s, giving per-pixel signal-to-noise ratios as high as 120 (more typically ∼60) near 5500 Å. We reduced the spectra using standard IRAF tasks and measured relative RVs from the spectra using the same methodology as we used for the TRES data. The resulting measurements are shown in Figure 3 and tabulated in Table 3.

2.3.3. PEPSI Spectra

We obtained high-resolution spectra of KELT-21 with $R = \lambda/\Delta\lambda = 120{,}000$ with the PEPSI (Strassmeier et al. 2015) spectrograph at the 2 × 8.4 m Large Binocular Telescope (LBT) on Mt. Graham, Arizona, USA. PEPSI is a fiber-fed white-pupil échelle spectrograph with two arms (blue and red optimized). We employed two of the six cross dispersers (CD II and CD IV), which covered the wavelength ranges 4265–4800 Å and 5441–6278 Å simultaneously. The instrument is stabilized in a pressure- and temperature-controlled chamber and is fed by three pairs of octagonal fibers per LBT unit telescope (for overall performance characterization, we refer to Strassmeier et al. 2017). For the present observations, we used the 200 μm core fibers and the five-slice image slicer to achieve the spectral resolution of 120,000. The spectra are sampled with 4.2 pixels per resolution element. The fiber core projection on the sky is 1.″5. The spectrum is recorded by two 10.3k × 10.3k STA1600LN CCDs with 9 μm pixels.

The observations occurred on 2017 May 29 UT and lasted for 4 hr, concluding when we had to close for sunrise. We set the integration time to 1200 s. CCD readout and overhead sums to 90 s and enabled a sequence of 13 back-to-back spectra. The target altitude was very low at the beginning of the observing sequence with an airmass of ∼2.1. The sky was clear and seeing at the start of the sequence was 1.″0 but deteriorated to 1.″3 at the end of the sequence. Peak signal-to-noise ratios were 140 and 100 per pixel in CD IV and CD II, respectively.

Data reduction was done with the software package SDS4PEPSI ("Spectroscopic Data Systems for PEPSI"), based on Ilyin (2000) and described in more detail in Strassmeier

Table 3
Radial Velocities of KELT-21

BJD_{TDB}	RV (km s^{-1})	σ_{RV} (km s^{-1})	Phase	Instrument
2456902.88217	−8.88	1.31	0.20	TRES
2457642.70515[a]	−9.87	0.50	0.98	TRES
2457642.73542[a]	−8.96	0.94	0.99	TRES
2457902.80358[a]	−9.67	0.71	0.98	TRES
2457902.82614[a]	−8.61	1.36	0.99	TRES
2457902.84897[a]	−10.26	2.28	0.99	TRES
2457902.87114[a]	−10.80	1.00	1.00	TRES
2457902.89397[a]	−11.51	0.62	0.00	TRES
2457902.91618[a]	−11.03	0.62	0.01	TRES
2457902.93846[a]	−12.27	0.91	0.02	TRES
2457902.96073[a]	−11.17	0.61	0.02	TRES
2457903.94587	−11.25	0.75	0.30	TRES
2457905.81193	−11.11	0.75	0.81	TRES
2457910.86090	−10.84	0.58	0.21	TRES
2457913.82452	−10.52	0.53	0.03	TRES
2457914.86709	−9.77	0.53	0.32	TRES
2457915.95596	−11.01	0.50	0.62	TRES
2457916.89286	−10.86	0.50	0.88	TRES
2457917.95251	−11.23	1.21	0.17	TRES
2457919.91707	−10.92	0.52	0.72	TRES
2457686.57439	−9.75	1.62	0.13	TS23
2457686.71975	−10.86	0.93	0.17	TS23
2457687.58795	−9.83	0.81	0.41	TS23
2457732.56483	−9.48	1.60	0.86	TS23
2457734.59627	−10.45	0.68	0.42	TS23
2457735.58946	−10.71	1.23	0.69	TS23
2457736.57659	−15.99	1.96	0.97	TS23
2457919.93596	−10.01	2.78	0.72	TS23
2457920.92942	−10.71	1.48	1.00	TS23
2457921.91076	−10.59	1.27	0.27	TS23
2457922.93250	−9.49	1.89	0.55	TS23
2457923.91227	−10.44	1.86	0.82	TS23

Note. See Table 5 for the RV zeropoint values. We have assumed a minimum uncertainty of 0.5 km s^{-1} on the RV measurements.
[a] Denotes that the observation takes place during transit and was excluded from our RV analysis (although the spectra from BJD 2457902 were used in our Doppler tomographic analysis; Section 4.1).

et al. (2017). It relies on the adaptive selection of parameters by using statistical inference and robust estimators. The standard reduction steps include bias overscan detection and subtraction, scattered light extraction from the interorder space and subtraction, definition of échelle orders, optimal extraction of spectral orders, wavelength calibration, and a self-consistent continuum fit to the full 2D image of extracted orders. Our Doppler tomographic analysis of these spectra is described in Section 4.1.

2.4. High-contrast AO Imaging

We obtained adaptive optics (AO) images of KELT-21 on 2017 June 12 UT using the NIRC2 instrument on Keck II, Maunakea, Hawaii, USA. The observing conditions were excellent. KELT-21 was observed at an airmass of $\sec z = 1.07$ with seeing estimated to be $\sim 0\farcs 3$. The narrow camera mode was used to provide a plate scale of 9.942 ± 0.05 mas pix^{-1}. A three-point dither pattern was implemented to avoid the noisy quadrant of the NIRC2 detector. A total of 30 frames were recorded using position angle mode in the K_s band; the sequence resulted in a total integration time of 30 seconds. No off-axis sources were identified in raw frames, so we did not obtain images in complementary filters. Later inspection of processed frames, however, revealed two faint companions to the south of KELT-21 (top panel of Figure 4).

Standard AO imaging reduction methods were used to flat-field the images, correct for bad pixels, and subtract the sky background (Crepp et al. 2012). Upon noticing the companions from the NIRC2 automated pipeline, we performed several experiments to confirm their nature, including studying how the signal-to-noise ratio improved with increasing number of processed frames from different detector quadrants. We also carefully assessed image registration internal to the pipeline to ensure that virtual copies of the primary star or other effects were not creating multiple off-axis signals. Finally, a contrast curve was generated to serve as a self-consistency check for the detected companions' flux levels and limit the existence of other sources near KELT-21 (bottom panel of Figure 4). In order to construct the contrast curve, we divide the image into a grid with a cell size set to the FWHM of the PSF and calculate the rms over each 3×3 set of cells. The contrast curve denotes the 5σ median-combined rms value azimuthally averaged over the 3×3 cells centered at a given radial separation from KELT-21. The companions are more than a magnitude above the contrast curve, indicating that their detection is secure, and we do not detect any other sources of comparable or greater brightness near KELT-21.

Although well-separated from the primary star by just over an arcsecond, the two sources themselves have comparable flux and are only marginally spatially resolved. Utilizing brute-force modeling of the companions as a combined source using aperture photometry, we find a combined magnitude difference of $\Delta K_s = 6.39 \pm 0.06$ compared to the primary star. We then employed Markov Chain Monte Carlo (MCMC) methods to compute the relative brightness and astrometric positions of the closely separated binary pair. To disentangle the contribution of each source, we use the technique described in Bechter et al. (2014) to self-consistently fit the AO data. Specifically, we model the core and halo of each source using a modified Moffat function that includes nuisance parameters such as the residual

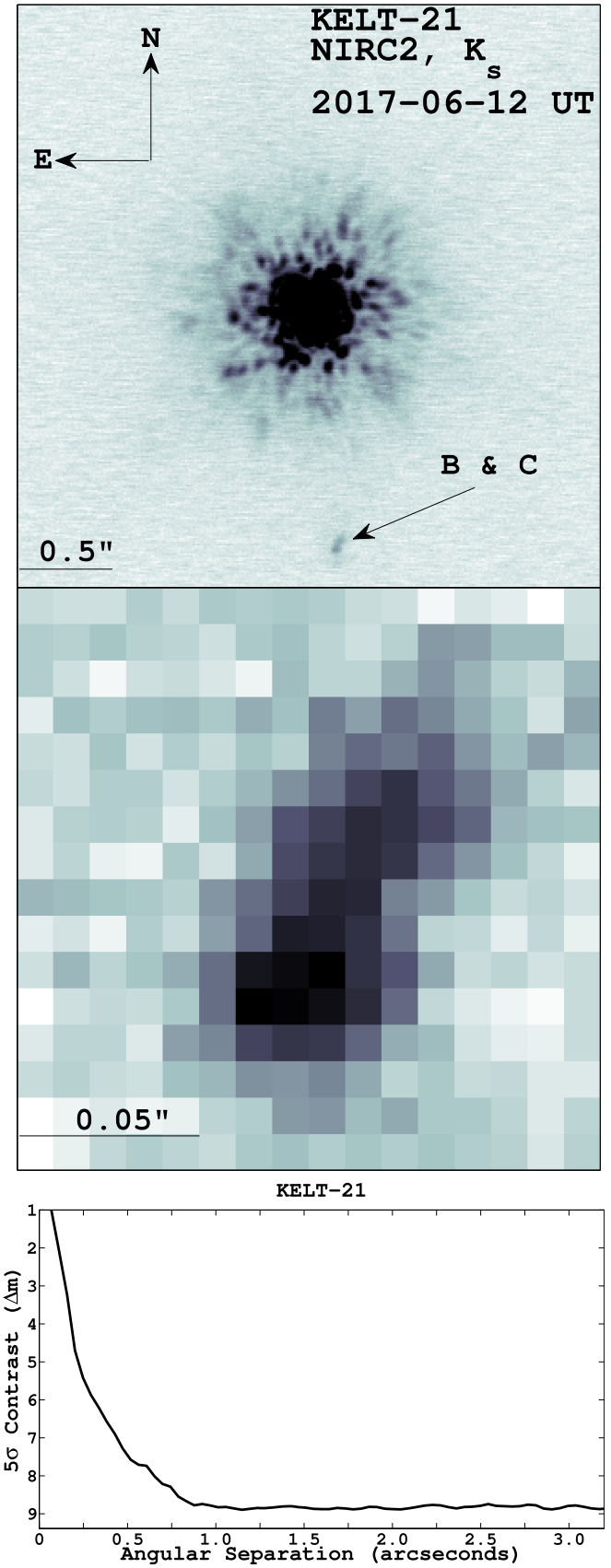

Figure 4. Top: Keck NIRC2 AO image of the KELT-21 system, showing the primary star and the two faint companions B and C. Middle: zoom-in on the companions B and C. Bottom: contrast curve for these observations.

Table 4
Properties of the Likely Companions KELT-21 B and C

Parameter	Description (Units)	Value
KELT-21 B		
ρ_{AB}	Separation (mas)	1261 ± 12
PA_{AB}	Position Angle (degrees, east of north)	185.3 ± 0.1
ΔK_s	Contrast (mag)	7.00 ± 0.06
$a_{\perp,AB}$	Projected Separation (au)	523 ± 62
M_B	Estimated Mass ($M_\odot$)	$0.13^{+0.02}_{-0.01}$
KELT-21 C		
ρ_{AC}	Separation (mas)	1214 ± 14
PA_{AC}	Position Angle (degrees, east of north)	186.6 ± 0.1
ΔK_s	Contrast (mag)	7.30 ± 0.06
$a_{\perp,AC}$	Projected Separation (au)	504 ± 60
M_C	Estimated Mass ($M_\odot$)	0.11 ± 0.01
KELT-21 BC		
ρ_{BC}	Separation (mas)	55 ± 16
PA_{BC}	Position Angle (degrees, east of north)	324 ± 10
ΔK_s	Contrast (mag)	0.30 ± 0.08
$a_{\perp,BC}$	Projected Separation (au)	22.9 ± 7.1

Note. All parameters are quoted at the epoch of the observations, 2017 June 12 UT. Subscripts AB, AC, and BC refer to mutual parameters between stars A (the planet-host star KELT-21) and B, A and C, and B and C, respectively. The physical parameters of KELT-21 B and C are calculated assuming that they are physically associated with KELT-21; see Section 5.2. The quoted uncertainties on these parameters are calculated given the formal uncertainties on the parameters of KELT-21 and the photometric measurements but ignore sources of systematics such as uncertainties in stellar isochrones.

sky background pedestal. After numerically identifying the multidimensional parameter space global minimum, we ran one million iterations to generate posterior distributions that quantify the relative position and brightness of the putative companions and their uncertainties. Results are shown in Table 4. We will consider the candidate companions in more detail in Section 5.2.

3. Host Star Characterization

3.1. SED Analysis

We followed the approach of previous KELT discoveries and fitted the broadband spectral energy distribution (SED) of KELT-21 using a Kurucz (1992) atmosphere model. We adopted the broadband fluxes from the available all-sky photometric catalogs, in particular B_T and V_T from Tycho-2, JHK_S from 2MASS, and *WISE*1–3 from AllWISE. We also adopted the *Gaia* DR1 parallax, $\pi = 2.41 \pm 0.28$ mas, corrected for the systematic offset determined by Stassun & Torres (2016). These data are listed in Table 1. The free parameters of the fit were $T_{\rm eff}$ and the extinction, A_V, limited by the maximum line-of-sight A_V from the Schlegel et al. (1998) dust maps. Since $\log g_*$ and [Fe/H] are of secondary importance to the SED, we assumed a main-sequence $\log g_* = 4$ and solar metallicity. We ignored the presence of the candidate companions discussed in Section 2.4 as they are much fainter than KELT-21 (combined $\Delta K_S = 6.39 \pm 0.06$) and so should have a negligible effect on the SED.

The best-fit SED has $\chi^2_\nu = 4.2$ for five degrees of freedom. The best-fit parameters are $T_{\rm eff} = 8000^{+1000}_{-250}$ K and $A_V = 0.00^{+0.34}_{-0.00}$. Integrating the SED gives an extinction-corrected bolometric flux at Earth of $F_{\rm bol} = 1.61^{+0.78}_{-0.13} \times 10^9$ erg s^{-1} cm^{-2}.

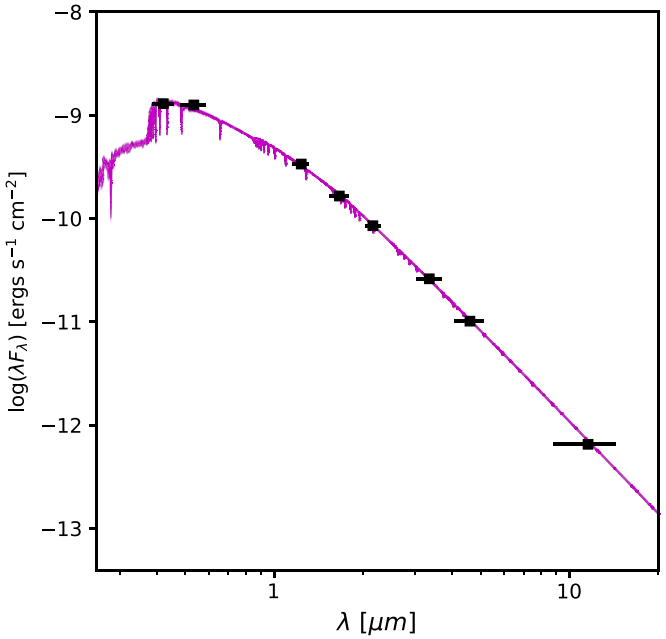

Figure 5. Spectral energy distribution of KELT-21. The purple line shows the best-fit model from The Payne and 50 random draws from the posteriors (only visible as a finite width to the line), and the black points show the literature photometry used. The error bars on each point represent the width of each photometric band.

3.2. Spectroscopic Analysis

We determined the properties of KELT-21 using The Payne, a newly developed approach for determining stellar parameters from simultaneously fitting the observed spectrum and SED self-consistently with ab initio models. The basic framework of The Payne algorithm is given in Ting et al. (2016) and Rix et al. (2016), and full details of the code will be given in P. A. Cargile et al. (2018, in preparation).

Using The Payne, we model five of the individual TRES spectra of KELT-21. In the inference, we fit a wavelength region of ∼200 Å around the Mg I (Mg b) triplet at ∼5200 Å, and all available photometry from the Tycho-2, 2MASS, and AllWISE catalogs (Table 1); we did not use the AllWISE *W*4 band as there is only a limit available in *W*4. For each TRES spectrum, we infer the most probable $T_{\rm eff}$, $\log g_*$, [Fe/H], [α/Fe], RV, intrinsic stellar broadening, instrumental broadening profile, stellar radius, distance, and extinction in the *V* band (A_V). We apply priors on the known instrumental profile for the TRES instrument ($R = 44{,}000$), the *Gaia* DR1 parallax distance ($\Pi = 2.41 \pm 0.28$ mas), and the surface gravity inferred from the planetary transit model ($\log g_* = 4.16 \pm 0.1$; see Section 4.2).

In order to determine the overall best-fit stellar parameters for KELT-21, we take the median and standard deviation of the results from the modeling of the five individual spectra. We note that the standard deviation of the five TRES spectra is very similar to the measurement errors on the most probable fit for the individual spectra, suggesting that it is a good representation of the formal measurement uncertainties from The Payne. We show the best-fit SED in Figure 5.

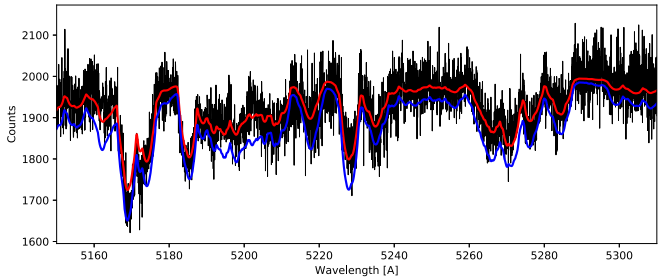

Figure 6. A section of one TRES spectrum of KELT-21, showing the data in black, the best-fit model from The Payne (with [Fe/H] $= -0.410 \pm 0.032$, [α/Fe] $= 0.145 \pm 0.053$) in red, and a model with the same stellar parameters except [Fe/H] $= 0.0$, [α/Fe] $= 0.0$ in blue. It is visually apparent that the low-metallicity, α-enhanced model is a better fit to the data—the solar-metallicity model generally overpredicts the line depths—and so we conclude that the low metallicity of KELT-21 is robust despite the rapid stellar rotation.

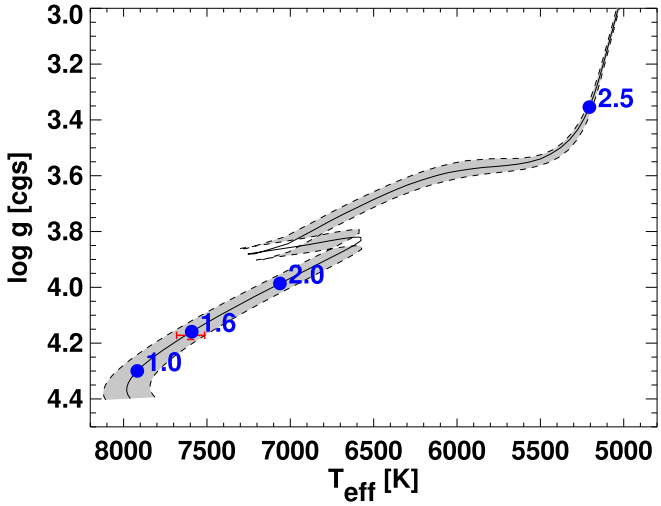

Figure 7. Location of KELT-21 in the Kiel diagram. The best-fit $T_{\rm eff}$ and $\log g_*$ from the global model fit is shown as the red point, while the gray swath shows a Yonsei–Yale evolutionary track for a star with the best-fit values of M_* and [Fe/H]; the locations on the best-fit model corresponding to several values of the stellar age are shown as the blue points, with ages quoted in gigayears.

Our analysis with The Payne produced stellar parameters of $T_{\rm eff} = 7587 \pm 82$ K, [Fe/H] $= -0.410 \pm 0.032$, [α/Fe] $= 0.145 \pm 0.053$, and $v \sin I_* = 144.3 \pm 1.2$ km s^{-1}. The uncertainties on our metallicity and α-enhancement measurements are small, which is somewhat surprising given the difficulty of spectral analysis for hot, rapidly rotating stars like KELT-21. Nonetheless, we argue that the subsolar metallicity is robust. In Figure 6, we show part of one of our TRES spectra, along with the best-fit model and a model with solar metallicity. The solar-metallicity model consistently overpredicts the depths of the spectral lines. Additionally, solutions with [Fe/H] $= 0$, [α/Fe] $= 0$ have posterior probabilities of $\sim 10^{-8}$–10^{-10} (as do solutions with either [Fe/H] $= 0$ or [α/Fe] $= 0$ individually) in most of our fits with The Payne. We thus conclude that KELT-21 is indeed metal poor, which is unusual for relatively young (<2 Gyr), hot stars; we explore the implications of this measurement in more detail in Section 5.3. Additionally, the $T_{\rm eff}$ value found here is 1.6σ discrepant from that found in our SED analysis in Section 3.1. This is likely due to the fact that our SED-only analysis assumed [Fe/H] $= 0$, which is not the case; our analysis with The Payne provides an equally good fit to the literature photometry, and so we proceed using these stellar parameters. The Payne value of $v \sin I_*$ is mostly consistent (1.3σ difference) with that measured independently from the PEPSI spectra (Section 4.2).

A $T_{\rm eff}$ of 7587 K corresponds to a spectral type of A8, per the $T_{\rm eff}$–spectral type calibration of Pecaut & Mamajek (2013), while the surface gravity value of $\log g_* = 4.173^{+0.016}_{-0.015}$ from the global fit (Section 4.2) indicates that KELT-21 is on the main sequence. We therefore find a spectral type of A8V for KELT-21; this is one of only a handful of A stars known to host a transiting planet.

3.3. Evolutionary Analysis

In Figure 7, we show KELT-21 in the $T_{\rm eff}$–$\log g_*$ plane, i.e., the Kiel diagram, along with a Yonsei–Yale (YY; Demarque et al. 2004) evolutionary track for the mass and [Fe/H] of KELT-21. The evolutionary track implies an age of $\sim 1.6 \pm 0.1$ Gyr for KELT-21. KELT-21 will start evolving off the main sequence within the next few hundred million years, and within $\sim$1 Gyr it will begin ascending the red giant branch.

3.4. UVW Space Motion and Galactic Location

In order to put the KELT-21 system into a broader Galactic context, we calculated its three-dimensional Galactic space motion (U, V, W). We obtained the proper motion and parallax of KELT-21 from *Gaia* DR1 (*Gaia* Collaboration et al. 2016) and corrected the parallax for systematic biases per the formulation of Stassun & Torres (2016). We also used the absolute RV of the system on the IAU scale as determined from our TRES spectra (Section 2.3.1). All of these parameters are listed in Table 1.

We calculated the Galactic space motion using the IDL routine `GAL_UVW`,[48] which is based upon the methodology of Johnson & Soderblom (1987), and we used the value of the solar velocity with respect to the local standard of rest found by Coşkunoğlu et al. (2011). We find that KELT-21 has a space motion of (U, V, W) $= (9.2 \pm 1.9, -0.5 \pm 1.1, 8.9 \pm 1.9)$ km s^{-1}; we use the coordinate system such that the Galactic center is in the direction of positive U. Using the criteria of Bensby et al. (2003), this corresponds to a 99.4% probability that KELT-21 is a member of the Milky Way's thin disk. This is expected given the relatively high mass, and therefore relatively low age, of KELT-21. We note that the Bensby et al. (2003) criteria are not strictly applicable to KELT-21, as they were derived for the solar neighborhood, and KELT-21 is located at a distance of 0.4 kpc. KELT-21 is located close to the solar circle, however (as $l = 71.^\circ4814$, $b = -1.^\circ9865$), suggesting that the Bensby et al. (2003) criteria are likely not unreasonable. Indeed, our integration of the orbit of KELT-21 (Section 5.3) confirms its thin-disk kinematics.

Given that KELT-21 is located very close to the Galactic plane, significant extinction and reddening might be expected. The Pan-STARRS 1 dust map[49] (Green et al. 2015) predicts a reddening of $E(B-V) = 0.09^{+0.02}_{-0.03}$ at the distance and position of KELT-21, although this is close enough that there are not enough stars for the dust map to be fully reliable. Using a standard value of $R_V = 3.1$, this corresponds to an expected extinction of $A_V = 0.28^{+0.06}_{-0.09}$, which is consistent to within 1σ with the value of $A_V = 0.00^{+0.34}_{-0.00}$ found in our SED analysis (Section 3.1). The PEPSI spectra also show significant

[48] https://idlastro.gsfc.nasa.gov/ftp/pro/astro/gal_uvw.pro
[49] http://argonaut.skymaps.info/

interstellar absorption with a complex velocity structure in the Na I D lines, as is expected for a star in this direction and distance.

4. Planet Characterization

4.1. Doppler Tomographic Characterization

We analyzed the PEPSI and in-transit TRES data using Doppler tomographic methodology. When a planet transits a rotating star, the obscured regions of the stellar disk do not contribute to the formation of the rotationally broadened stellar absorption line profile. The subtracted light results in a perturbation to the line profile at velocities corresponding to the radial velocities of the obscured surface elements. This is known as the Rossiter–McLaughlin effect (Rossiter 1924; McLaughlin 1924). For slowly rotating stars, this is typically interpreted as an anomalous RV shift during the transit due to the changing line centroids (e.g., Triaud et al. 2010). For sufficiently rapid rotation and/or sufficiently high spectral resolution, however, we can spectroscopically resolve the rotationally broadened line profile and the line profile perturbation. This is Doppler tomography (e.g., Collier Cameron et al. 2010; Johnson et al. 2014). Detection of the line profile perturbation confirms that the planet candidate does indeed transit the target rapidly rotating star. Furthermore, the motion of the line profile perturbation across the line profile during the transit is diagnostic of the spin–orbit misalignment λ, which is the angle between the stellar spin and planetary orbital angular momentum vectors projected onto the plane of the sky.

Our procedure to extract the time series line profiles from the PEPSI data is essentially the same as that used by Johnson et al. (2014, 2015, 2017). In short, we use least-squares deconvolution (Donati et al. 1997) to extract the average line profile from each spectrum. We use a line mask with initial guesses for the line depths taken from a Vienna Atomic Line Database (VALD; Ryabchikova et al. 2015) stellar model with the stellar parameters of KELT-21; best-fit line depths are then found using the stacked PEPSI spectra before the final line profiles are extracted.

One modification from earlier methodology is necessary because of the narrower bandwidth of PEPSI with respect to the spectrographs used by Johnson et al. (2014, 2015, 2017). A significant fraction of the PEPSI blue arm spectrum is occupied by the Hγ line and its wings. Rather than entirely excluding this region of the spectrum, as was done in the vicinity of strong lines by Johnson et al. (2014, 2015, 2017), we instead subtract off a model of the Hγ line profile from Kurucz (1979),[50] The PEPSI red arm spectrum has very few lines strong enough to use for the Doppler tomographic analysis; we only utilize a few lines blueward of 5680 Å, while the Na I D lines are not usable as they suffer from strong interstellar contamination. We show the extracted time series line profile residuals, displaying the planetary transit, in the top-left panel of Figure 8.

For the TRES Doppler tomographic observations, we calculate a line broadening kernel from each transit spectrum as per the least-squares deconvolution process described in Section 2.3.1. To detect the tomographic shadow of the transiting planet, we subtract the out-of-transit broadening kernel from the in-transit kernels (Collier Cameron et al. 2010; Zhou et al. 2016a). The residuals, showing the transit signal, are shown in the upper-right panel of Figure 8.

By inspection, it is apparent that the planetary orbit is prograde and well-aligned, as the line profile perturbation moves from the blueshifted to the redshifted limb during the course of the transit, and spans nearly the full velocity range of $\pm v \sin I_*$. Our global fit (Section 4.2) confirms this qualitative assessment: we obtain $\lambda = -5.6^{+1.7}_{-1.9}$°. The implications of this measurement are discussed in Sections 5.1 and 5.2.3.

4.2. EXOFAST Global Fit

To measure the system parameters for KELT-21, we simultaneously fit all photometric and spectroscopic (including Doppler tomographic) data using a heavily modified version of EXOFAST (Eastman et al. 2013). To determine the radius and mass of KELT-21, we use either the YY stellar evolutionary tracks (Demarque et al. 2004) or the Torres empirical relations (Torres et al. 2010). We conduct two separate global fits (YY and Torres) with the eccentricity of the planet's orbit set to zero. We assume a circular orbit as our RV measurements are unable to measure the planetary mass, let alone provide meaningful constraints on the orbital eccentricity, and hot Jupiters also typically have circular or nearly circular orbits due to strong tidal damping. For a detailed description of the global modeling process, see Siverd et al. (2012). We use the SED + spectroscopic fit-determined $T_{\rm eff}$ of 7587 ± 82 K and [Fe/H] of −0.410 ± 0.032 (Section 3.2) as a prior. From an analysis of the KELT-North light curve, we add a prior on the period and transit center time. We also included priors of $v \sin I_* = 146.0 \pm 0.5\,{\rm km\,s^{-1}}$ and a width of a Gaussian non-rotating line profile of $5.2 \pm 0.8\,{\rm km\,s^{-1}}$ derived from a preliminary fit to the PEPSI line profiles (Section 4.1) using the line profile model described in Johnson et al. (2014).

After the global fit (both YY and Torres), we measure an independent ephemeris from a linear fit of the determined transit center times for each follow-up light curve. We then re-ran both fits using this new T_c and period and their uncertainties as priors to obtain the final results. We do not include the KELT-North light curve in any of the global fits due to difficult-to-quantify blending. We also place a prior on R_* of $1.53 \pm 0.43\ R_\odot$ using the *Gaia* parallax (see Table 1) and the measured bolometric flux from our SED analysis (Section 3.1). We adopt the YY fit for the discussion of the KELT-21 system. See Tables 5 and 6 for the results of both global fits.

We ignored any contribution of the candidate companions described in Section 2.4 to the photometric data or the spectra. Based upon the ΔK_S contrast values from the AO data and assuming physical association of the companions with KELT-21 (see Section 5.2), we estimate flux ratios between the exoplanet host star and the combined light of the companions of 1.5×10^{-4} in the V band and 3.3×10^{-4} in the I_C band. Not accounting for this flux would cause a systematic underestimate in the transit depth much less than the uncertainty due to photometric noise, and so we can safely ignore this contaminating flux. We also note that this implies that the companions are too faint to cause the transit signal if one of them were to be an eclipsing binary (a possibility that is also excluded by our detection of the Doppler tomographic transit signal).

[50] As tabulated at http://kurucz.harvard.edu/grids/gridm01/bm01k2.datcd.

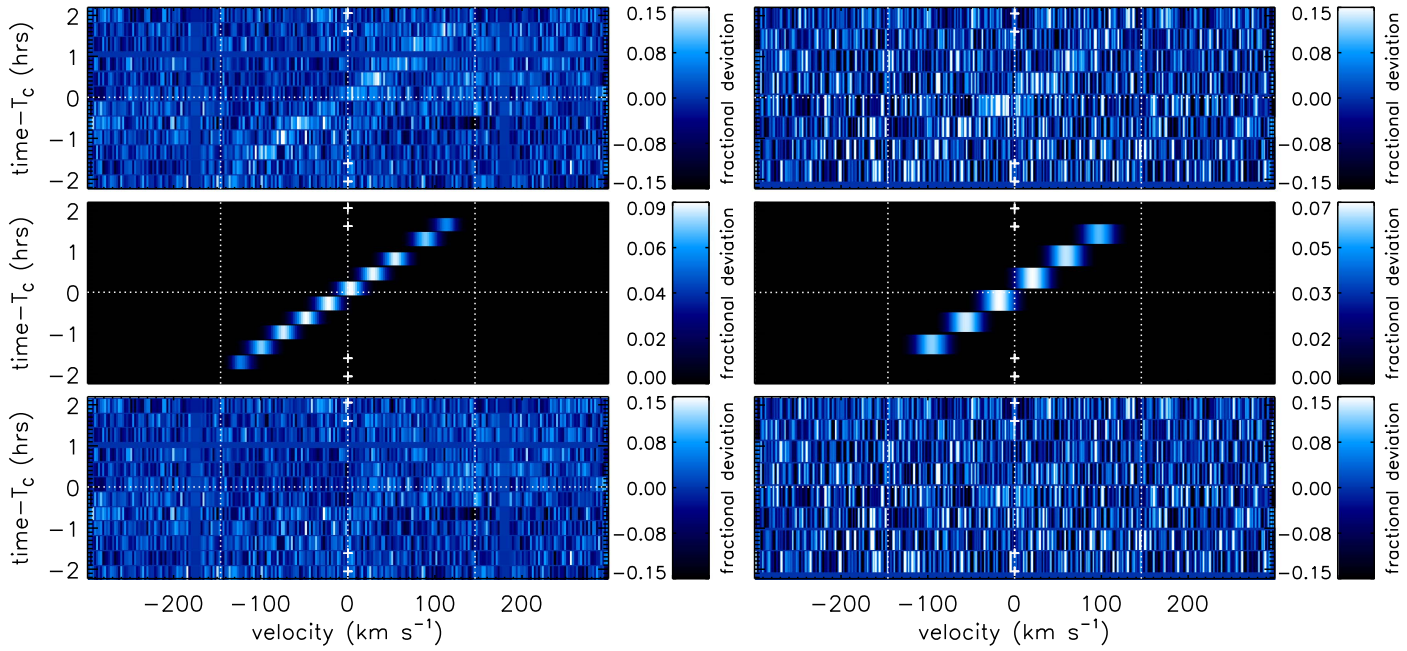

Figure 8. Doppler tomographic data for KELT-21. The PEPSI observations are shown in the left column and the TRES observations in the right column. The top row shows the data, the middle row the best-fit model of the line profile perturbation due to the transit, and the bottom row the residuals after subtraction of the best-fit model. In all panels, time increases from bottom to top, and each color-scale row shows the deviation of the line profile at that time from the average line profile. The transit is the bright streak moving from lower left to upper right. Vertical lines mark the center of the line profile at $v = 0$ and the edges at $v = \pm v \sin I_*$, a horizontal line shows the time of mid-transit, and the four small crosses depict the times of the first through fourth contacts. The data have been binned down by a factor of 4 in the velocity axis as compared to the raw data for display purposes to better show the transit; the full-resolution data were used in the global fits. All panels showing data use the same color-scale range for better comparison; all pixels outside this range have been set to these extreme values.

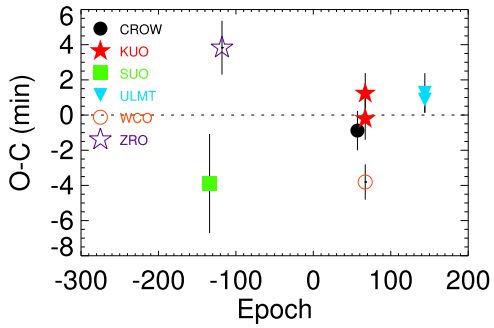

Figure 9. Transit time residuals for KELT-21b using the inferior conjunction time from the global fit to define the epoch. The data are listed in Table 7.

4.3. Transit Timing Variation Analysis

Using the fiducial global model determined transit center times (see Table 7), we searched for transit timing variations in the KELT-21 system. We ensure that all follow-up light curves are using $\mathrm{BJD_{TDB}}$ time stamps (Eastman et al. 2010). Additionally, all follow-up members synchronize their telescope control computers to a standard clock prior to observing. This is typically done periodically throughout an observing night. We perform a linear fit to the determined transit midtimes, obtaining a linear ephemeris of $T_0 = 2457382.640727 \pm 0.00041$ ($\mathrm{BJD_{TDB}}$) and $P = 3.6127628 \pm 0.0000038$ days, with $\chi^2 = 27.2$ and six degrees of freedom. These measurements are shown in Figure 9. Although several of the data points lie more than 1σ from the zero O–C line, two of the greatest outliers are the observations from SUO (large scatter) and ZRO (ingress only), which we would expect to have lower timing precision. Furthermore, the WCO observations are of the same transit as those observed by KUO, which show no deviations from the linear ephemeris. These deviations are likely due to the systematics inherent to ground-based transit timing observations (Carter & Winn 2009). We thus find no conclusive evidence for any astrophysical TTVs in our data and adopt this as the best ephemeris for predicting future transit times.

4.4. Tidal Evolution and Insolation History

Using the POET code (Penev et al. 2014), we followed the past and future tidal orbital evolution of the KELT-21 system under the constant phase lag (constant tidal quality factor) assumption. We incorporated the evolution of the stellar radius and luminosity, and followed the transfer of angular momentum from the star to the orbit. Note that in this case, the minimum equatorial velocity of the star (i.e., $v \sin I_*$) implies that the star is spinning super-synchronously; given the stellar radius and $v \sin I_*$ found in Section 4.2, $P_{\rm rot} < 0.57$ days, compared to $P = 3.61$ days for the planet. Thus, tidal dissipation causes the planet to move outward and the star to spin down. Calculations were performed with three different assumptions for the modified tidal quality factor of KELT-21: $Q'_* = 10^{6.03}$, 10^7, and 10^8 to demonstrate the range of plausible evolutions. The value of $Q'_* = 10^{6.03}$ was chosen as any smaller value of Q'_* would require the planet to be inside the star at an age of 200 Myr. Although tidal quality factors $>10^7$ are plausible, especially for "hot" stars like KELT-21, the orbital evolution on the main sequence is already small for $Q'_* = 10^7$, and differences in orbital evolution for $Q'_* = 10^7$ and 10^8 are thus minimal.

We show the evolution of the semimajor axis of KELT-21b in the top panel of Figure 10, and that of the stellar insolation received by KELT-21b in the bottom panel. The changes in semimajor axis and insolation are small for $Q'_* \geqslant 10^7$. For

Table 5
Median Values and 68% Confidence Interval for the Physical and Orbital Parameters of the KELT-21 System

Parameter	Description (Units)	Adopted Value (YY Circular)	Value (Torres Circular)
Stellar Parameters			
M_*	Mass ($M_\odot$)	$1.458^{+0.029}_{-0.028}$	$1.526^{+0.070}_{-0.067}$
R_*	Radius ($R_\odot$)	1.638 ± 0.034	1.663 ± 0.041
L_*	Luminosity ($L_\odot$)	$8.03^{+0.54}_{-0.53}$	$8.28^{+0.60}_{-0.58}$
ρ_*	Density (cgs)	$0.468^{+0.026}_{-0.024}$	$0.468^{+0.026}_{-0.024}$
$\log g_*$	Surface gravity (cgs)	$4.173^{+0.015}_{-0.014}$	4.180 ± 0.016
$T_{\rm eff}$	Effective temperature (K)	7598^{+81}_{-84}	7600^{+81}_{-84}
[Fe/H]	Metallicity	$-0.405^{+0.032}_{-0.033}$	-0.405 ± 0.032
$v \sin I_*$	Rotational velocity (km s^{-1})	146.03 ± 0.48	$146.03^{+0.49}_{-0.50}$
λ	Spin–orbit alignment (degrees)	$-5.6^{+1.7}_{-1.9}$	$-5.6^{+1.7}_{-1.9}$
NRVel.W.	Non-rotating line width (km s^{-1})	5.17 ± 0.48	5.09 ± 0.74
Planet Parameters			
P	Period (days)	3.6127647 ± 0.0000033	3.6127647 ± 0.0000033
a	Semimajor axis (au)	$0.05224^{+0.00035}_{-0.00034}$	$0.05304^{+0.00080}_{-0.00079}$
M_P	Mass ($M_{\rm J}$)	(<3.91)	(<4.07)
R_P	Radius ($R_{\rm J}$)	$1.586^{+0.039}_{-0.040}$	1.610 ± 0.045
ρ_P	Density (cgs)	(<1.24)	(<1.23)
$\log g_P$	Surface gravity	(<3.59)	(<3.59)
T_{eq}	Equilibrium temperature (K)	2051^{+29}_{-30}	2051 ± 29
Θ	Safronov number	$0.0048^{+0.025}_{-0.0039}$	$0.0050^{+0.026}_{-0.0041}$
$\langle F \rangle$	Incident flux (10^9 erg s^{-1} cm^{-2})	4.01 ± 0.23	$4.02^{+0.23}_{-0.22}$
Radial Velocity Parameters			
T_C	Time of inferior conjunction (BJD$_{\rm TDB}$)	$2457295.93434^{+0.00041}_{-0.00042}$	$2457295.93435 \pm 0.00042$
K	RV semi-amplitude (m/s)	(<399.6)	(<406.3)
$M_P \sin i$	Minimum mass ($M_{\rm J}$)	(<3.91)	(<4.07)
M_P/M_*	Mass ratio	(<0.0025)	(<0.0026)
u	RM linear limb darkening	$0.5413^{+0.0058}_{-0.0033}$	$0.5412^{+0.0054}_{-0.0032}$
$\gamma_{McDonald}$	km s^{-1}	-10.50 ± 0.36	$-10.51^{+0.37}_{-0.36}$
γ_{TRES}	km s^{-1}	$-10.72^{+0.17}_{-0.18}$	-10.71 ± 0.18
Linear Ephemeris from Follow-up Transits			
$P_{\rm Trans}$	Period (days)	3.6127628 ± 0.0000038	...
T_0	Linear ephemeris from transits (BJD$_{\rm TDB}$)	$2457382.640727 \pm 0.00041$	...

Note. 3σ limits are reported for KELT-21b's mass and parameters dependent on the planetary mass. The gamma velocity reported here uses an arbitrary zeropoint for the multi-order relative velocities. Uncertainties are based strictly on formal uncertainties on the input data and do not take into account systematic effects. The quoted stellar parameters are for the planet-host star KELT-21.

$Q'_* = 10^{6.03}$, the evolution is more rapid and KELT-21b would have needed to begin its life at the stellar surface, and so the actual value of Q'_* is likely to be larger than $10^{6.03}$. Since we used the 3σ upper mass limit of 3.91 $M_{\rm J}$ for these calculations, the value of Q'_* could be smaller if the planetary mass is smaller, and the orbital evolution would be smaller for lower planetary mass at fixed Q'_*. Regardless of the value of Q'_*, larger changes will begin occurring in a few hundred million years, when KELT-21 begins evolving off of the main sequence.

5. Discussion

5.1. Spin–Orbit Misalignment

With our Doppler tomographic observations, we measured the spin–orbit misalignment, λ, obtaining $\lambda = -5.6^{+1.7}_{-1.9}°$. This, however, is not the true obliquity of the planetary orbit, but rather this value projected onto the plane of the sky. The full three-dimensional spin–orbit misalignment ψ is a more physically meaningful quantity than λ, but its calculation requires knowledge not only of λ and the planetary orbital inclination i, but also the inclination of the stellar rotation axis I_*. The first two of these are straightforward to measure; the latter is not, and we cannot measure this quantity for KELT-21 using our existing data.

We can, however, set limits on ψ by making reasonable assumptions to limit I_*, as we did in Siverd et al. (2018) and Lund et al. (2017). We follow Iorio (2011) by assuming that KELT-21 must be rotating at less than the break-up velocity, which must limit I_*, since the equatorial velocity is $v_{\rm eq} = v \sin I_* / \sin I_*$. Doing so with our best-fit values for the system parameters, we obtain a break-up velocity of $v_{\rm eq,max} = 232.5 \pm 3.3\,{\rm km\,s^{-1}}$, stellar inclination of $38.^\circ2 < I_* < 141.^\circ8$, and true orbital obliquity of $3.^\circ7 < \psi < 55.^\circ9$; the latter two ranges at 1σ confidence. Although KELT-21b certainly has a prograde orbit, we cannot exclude the possibility

Table 6
Median Values and 68% Confidence Intervals for the Physical and Orbital Parameters for the KELT-21 System

Parameter	Description (Units)	Adopted Value (YY circular)	Value (Torres circular)
Primary Transit			
R_P/R_*	Radius of the planet in stellar radii	$0.09952^{+0.00071}_{-0.00073}$	$0.09951^{+0.00070}_{-0.00071}$
a/R_*	Semimajor axis in stellar radii	$6.86^{+0.13}_{-0.12}$	$6.86^{+0.13}_{-0.12}$
i	Inclination (degrees)	$86.46^{+0.38}_{-0.34}$	$86.46^{+0.38}_{-0.34}$
b	Impact parameter	$0.423^{+0.033}_{-0.039}$	$0.423^{+0.033}_{-0.039}$
δ	Transit depth	0.00990 ± 0.00014	0.00990 ± 0.00014
$T_{\rm FWHM}$	FWHM duration (days)	$0.15242^{+0.00062}_{-0.00061}$	$0.15241^{+0.00062}_{-0.00063}$
τ	Ingress/egress duration (days)	0.01864 ± 0.00076	$0.01863^{+0.00076}_{-0.00075}$
T_{14}	Total duration (days)	$0.17106^{+0.00091}_{-0.00092}$	$0.17104^{+0.00093}_{-0.00091}$
P_T	A priori non-grazing transit probability	$0.1313^{+0.0022}_{-0.0023}$	0.1313 ± 0.0023
$P_{T,G}$	A priori transit probability	$0.1603^{+0.0028}_{-0.0030}$	0.1603 ± 0.0029
u_{1I}	Linear limb darkening	$0.1486^{+0.012}_{-0.0070}$	$0.1487^{+0.011}_{-0.0069}$
u_{2I}	Quadratic limb darkening	$0.3067^{+0.0099}_{-0.012}$	$0.3065^{+0.0098}_{-0.012}$
$u_{1\rm Sloang}$	Linear limb darkening	$0.3475^{+0.0068}_{-0.0040}$	$0.3472^{+0.0063}_{-0.0039}$
$u_{2\rm Sloang}$	Quadratic limb darkening	$0.3442^{+0.0014}_{-0.0023}$	$0.3444^{+0.0013}_{-0.0021}$
$u_{1\rm Sloani}$	Linear limb darkening	$0.1662^{+0.013}_{-0.0078}$	$0.1663^{+0.012}_{-0.0077}$
$u_{2\rm Sloani}$	Quadratic limb darkening	$0.3123^{+0.0100}_{-0.012}$	$0.3122^{+0.0099}_{-0.012}$
$u_{1\rm Sloanr}$	Linear limb darkening	$0.2277^{+0.012}_{-0.0076}$	$0.2277^{+0.011}_{-0.0076}$
$u_{2\rm Sloanr}$	Quadratic limb darkening	$0.3370^{+0.0079}_{-0.0100}$	$0.3369^{+0.0079}_{-0.0095}$
u_{1V}	Linear limb darkening	$0.2901^{+0.011}_{-0.0072}$	$0.2900^{+0.011}_{-0.0071}$
u_{2V}	Quadratic limb darkening	$0.3365^{+0.0053}_{-0.0074}$	$0.3365^{+0.0053}_{-0.0070}$
Secondary Eclipse			
T_S	Predicted time of eclipse ($\rm BJD_{TDB}$)	$2457294.12796^{+0.00041}_{-0.00042}$	$2457294.12796 \pm 0.00042$

Note. Uncertainties are based strictly on formal uncertainties on the input data and do not take into account systematic effects.

Table 7
Transit Times from KELT-21b Photometric Observations

Epoch	T_C ($\rm BJD_{TDB}$)	σ_{T_C} (s)	O–C (s)	O–C (σ_{T_C})	Telescope
−134	2456898.527802	169	−233.74	−1.38	SUO
−118	2456956.337374	91	229.94	2.50	ZRO
57	2457588.567597	67	−52.87	−0.79	CROW
67	2457624.696694	69	74.02	1.07	KUO
67	2457624.695694	72	−12.38	−0.17	KUO
67	2457624.693194	60	−228.38	−3.80	WCO
144	2457902.879452	67	75.71	1.13	ULMT
144	2457902.879181	45	52.30	1.16	ULMT

Note. Epochs are given in orbital periods relative to the value of the inferior conjunction time from the global fit.

that it is significantly misaligned with respect to the stellar rotation despite the alignment along the line of sight.

In Figure 11, we show the spin–orbit misalignments of all hot Jupiters for which this has been measured, along with KELT-21b. KELT-21 is well above the Kraft break, where hot Jupiters tend to have a wide range of misalignments (Winn et al. 2010). Although its well-aligned orbit is somewhat unusual in this context, some other hot Jupiters around hot stars are also aligned, such as KELT-7b (Zhou et al. 2016a) and KELT-20b/MASCARA-2b (Lund et al. 2017; Talens et al. 2017b). Even for an isotropic distribution of misalignments, some systems should be aligned by chance. Indeed, it is perhaps unsurprising that KELT-21, as the most rapidly rotating hot Jupiter host star known to date (bottom panel of Figure 11), possesses an apparently well-aligned planet. In

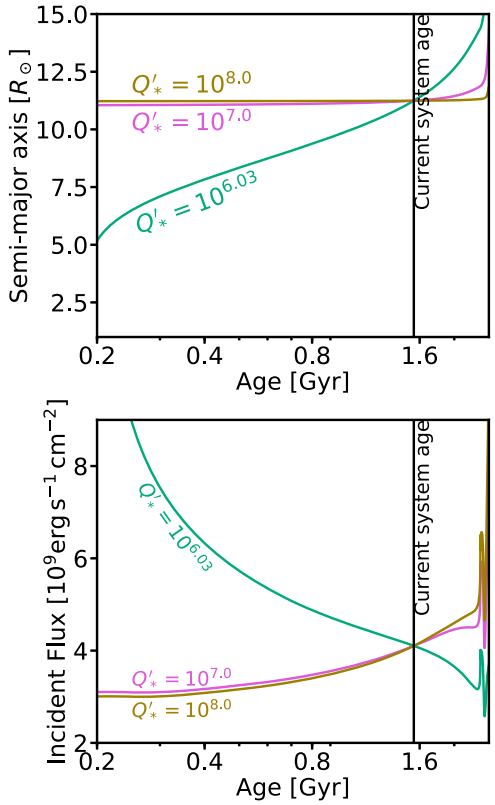

Figure 10. Predicted evolution of the (top) semimajor axis of and (bottom) stellar insolation experienced by KELT-21b under the influence of stellar tides. Teal, magenta, and dark yellow lines depict the evolution assuming a stellar tidal quality factor of $Q'_* = 10^{6.03}$, 10^7, and 10^8, respectively.

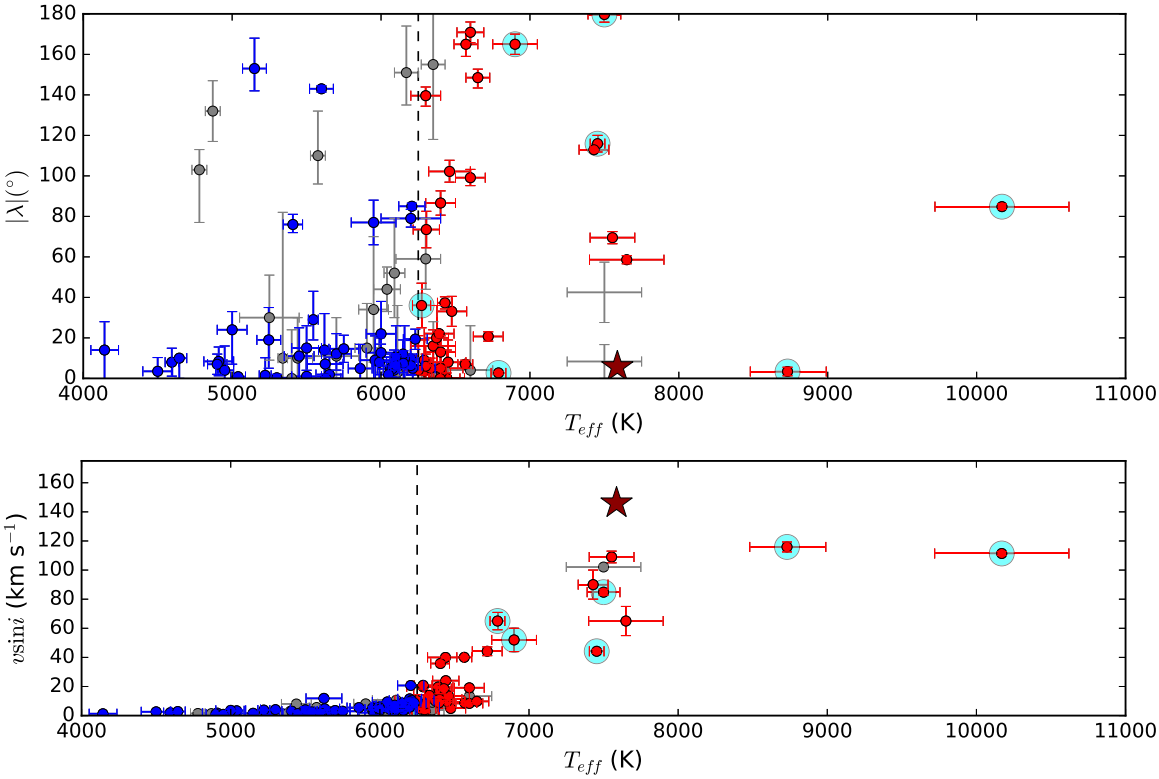

Figure 11. Top: distribution of the spin–orbit misalignments of hot Jupiters from the literature as a function of $T_{\rm eff}$, after Winn et al. (2010). Planets with host stars with $T_{\rm eff} < 6250$ K are shown in blue, those with $T_{\rm eff} > 6250$ K in red, and those with uncertainties of $>20^\circ$ on their reported values of λ in gray. A vertical dashed line denotes the approximate location of the Kraft break at 6250 K. Large cyan circles highlight planets discovered by the KELT survey, and KELT-21b is shown by the large dark red star; uncertainties on its parameters are smaller than the plot symbol size. HAT-P-57 is shown with the two sets of error bars without an associated plot point, denoting the two degenerate solutions found by Hartman et al. (2015). Bottom: $v \sin I_*$ values for these stars. The steady increase in average rotational velocity above the Kraft break is apparent. We assembled the literature sample using John Southworth's TEPCat Rossiter–McLaughlin Catalogue (http://www.astro.keele.ac.uk/jkt/tepcat/).

order for an aligned planet to transit, its host star must have $I_* \sim 90^\circ$, and so on average the $v \sin I_*$ values for aligned planets should be higher than those for misaligned planets (e.g., Schlaufman 2010; Winn et al. 2017).

The aligned orbit of KELT-21b suggests that it could have migrated to its current position through its protoplanetary disk, and that a dynamically hot migration mechanism, like planet–planet scattering (e.g., Lin et al. 1996) or the Kozai–Lidov mechanism (e.g., Fabrycky & Tremaine 2007; Naoz et al. 2012), is not required to explain KELT-21b. The value of $[{\rm Fe/H}] = -0.405^{+0.032}_{-0.033}$ that we have found is also interesting in the context of planet migration. Dawson & Murray-Clay (2013) found that hot and warm Jupiters orbiting lower-metallicity ($[{\rm Fe/H}] < 0$) stars typically have lower orbital eccentricities than those around higher-metallicity stars, and attributed this to disk migration for lower-metallicity stars and planet–planet scattering for higher-metallicity stars, which, due to the planet–metallicity correlation (e.g., Fischer & Valenti 2005), should form more giant planets. Planet–planet scattering should result in misaligned orbits, while disk migration should produce aligned orbits. That KELT-21, with $[{\rm Fe/H}] < 0$, has an aligned planet, could fit into this picture. On the other hand, the presence of possible stellar companions (Section 2.4) suggests that the Kozai–Lidov mechanism could still be responsible for the migration of KELT-21b; we discuss this possibility in more detail in Section 5.2.3.

5.2. KELT-21 as a Hierarchical Triple System

5.2.1. Are the Companions Bound?

Candidate stellar companions discovered through high-resolution imaging are typically confirmed to be bound to the primary star through the detection of common proper motion (e.g., Ngo et al. 2016). Alternately, if only a single epoch of photometry is available, multicolor photometry can be used to check that the secondary is consistent with being at the same distance as the primary (e.g., Evans et al. 2016). Finally, spectra can be used to determine whether the companion shares the systemic velocity of the primary (e.g., Siverd et al. 2018). We, however, have only a single epoch of single-color photometry of the candidate companions found in Section 2.4, and the candidate companions are too faint to be detected in our spectra. We cannot apply any of these methods to confirm or assess whether the companions are bound.

Instead, we follow a similar methodology to Oberst et al. (2017), who used source counts from 2MASS to argue that the probability of a chance alignment between KELT-16 with a star at least as bright as their candidate companion was small. The companions to KELT-21, however, are more than two magnitudes fainter in K_S than the companion to KELT-16 and are below the 2MASS completeness limit. We therefore used the same method as Oberst et al. (2017), but using star counts from a Galactic model rather than from actual data.

We generated Galactic models for the KELT-21 field using v1.6 of the TRILEGAL code[51] (Girardi et al. 2005) and with the Besançon code[52] (Robin et al. 2003). We generated a model for a 1 $\deg^2$ field centered on the location of KELT-21 ($l = 71\overset{\circ}{.}4814$, $b = -1\overset{\circ}{.}9865$). For TRILEGAL, we used the extinction from the Schlafly & Finkbeiner (2011) reddening maps at this location[53]; for the Besançon model, we used the dust map of Marshall et al. (2006). We assumed a binary fraction of 0.33 and flat mass ratio distribution between 0.2 and 1.0 after Raghavan et al. (2010), and otherwise used the default TRILEGAL and Besançon parameters. We ignore the contribution of the background galaxies as their source density is much smaller than that of stars near the Galactic plane. The source density of galaxies with $K < 17$ is $\mathcal{O}(10^3)$ $\deg^{-2}$ (e.g., Smith et al. 2009), while both TRILEGAL and Besançon predict a stellar source density of $\mathcal{O}(10^5)$ $\deg^{-2}$ in the same magnitude range. We counted the number of model sources brighter than the combined K_S magnitude of the companions ($K_S = 16.47$), and approximated the probability of a chance superposition as this total times the fraction of the 1 $\deg^2$ model area that is less than $1\farcs2$ from KELT-21 (this being the separation of the actual companions). This resulted in a probability of 3.8% (TRILEGAL) or 5.0% (Besançon) of a chance superposition. This suggests that the companions are likely to be bound, but the chance that they are background sources is too high to claim physical association with any certainty.

We can, however, further leverage the binary nature of the companion. First, we can assess the probability that the candidate companions are bound *to each other* using similar methodology. Here the probability of a chance superposition of an object brighter than $K_S = 17.38$ within 55 mas of the brighter candidate companion is 0.013% (TRILEGAL) or 0.019% (Besançon). We conclude that the companions are very likely to be bound to each other.

We can now assess the probability of the chance superposition of a *bound binary* close to KELT-21. To do so, we use the same TRILEGAL model as earlier, which accounts for the presence of binaries but does not contain any information on the separation of the binaries. For each binary in the TRILEGAL model, we drew a random orbital period from the log-normal distribution found by Raghavan et al. (2010) to approximate their results (mean of $\log P = 5.03$, standard deviation $\sigma_{\log P} = 2.28$), converted this to semimajor axis using Kepler's Third Law and the masses of the components from TRILEGAL, and computed a projected separation using the simplifying assumption of circular orbits and drawing a random orbital phase. We then calculated the magnitude difference ΔK_S between the components using the `isochrones` code (Morton 2015), assuming the age, masses, and metallicity of the system from TRILEGAL. We then assessed the total number of binary systems with projected separations larger than our resolution limit of $\lambda/D = 45$ mas, and smaller than the separation between KELT-21 and the candidate companions, and with a magnitude difference between the components smaller than that between the observed candidate companions. The Besançon model does not automatically include binaries, and so we randomly assigned binary companions to 33% of the model stars with a mass ratio drawn from a flat distribution over the interval $0.2 \leqslant q \leqslant 1$ and then otherwise followed the same methodology as for TRILEGAL. This indicates a probability of 0.035% (TRILEGAL) or 0.091% (Besançon) of the chance superposition of a background visual binary with KELT-21. We note that the choice of outer limit for this calculation has only a minimal effect on this result; 99% of the binaries with appropriate contrast ratios have separations of less than $0\farcs5$.

We thus conclude that the candidate companions are very likely to be bound to KELT-21, and for the remainder of this paper we assume that they are bound and refer to them as KELT-21B and KELT-21C. Future high-resolution imaging observations to confirm common proper motion of the companions will likely be difficult. The proper motion of KELT-21 is small (total proper motion of 2.34 ± 0.80 mas yr^{-1}; Table 1), and, indeed, is non-zero at only 2.9σ in TGAS (*Gaia* Collaboration et al. 2016). As is expected for a system close to the direction of Galactic rotation ($l = 71°$), the space motion of KELT-21 is primarily in the radial direction, resulting in small proper motion.

5.2.2. Properties of the Companions

Assuming that the companions are indeed physically bound to KELT-21, we can estimate their physical properties. In order to estimate the masses of the companions, we used the `isochrones` package (Morton 2015) to calculate the expected ΔK_S values between a primary with the properties of KELT-21 and the companions as a function of companion mass, which we compared to the observed values. This resulted in estimated companion masses of $M_B = 0.13^{+0.02}_{-0.01}$ $M_\odot$ and $M_C = 0.11 \pm 0.01$ $M_\odot$. The quoted uncertainties on these masses are derived purely from the uncertainties on the parameters of KELT-21 and on the photometric measurements, and ignore any systematic uncertainties from the isochrones or other sources. Using the M_*–spectral type relations of Pecaut & Mamajek (2013), these would correspond to spectral types of M5.5V and M6V for KELT-21 B and C, respectively.

Assuming $a \sim a_\perp$ (which is true on average; Heacox & Gathright 1994), the orbital periods of the B–C and A–BC binaries should be ~200 and ~9000 years, respectively. If the orbits were to be circular and face-on, this would correspond to an astrometric motion of A and BC due to their mutual orbit of ~120 and ~750 μas yr^{-1}, respectively, while the astrometric motion of B and C about each other would be ~800 μas yr^{-1}. *Gaia* should be able to achieve a proper motion precision of ~3–8 μas yr^{-1} on KELT-21,[54] and so should be able to easily detect its orbital motion in the A–BC binary. Components B and C should have *G*-band magnitudes of ~19.2 (using the relation between the *G*, *V*, and I_C magnitudes from Jordi et al. 2010), and *Gaia* should be able to achieve a parallax precision of 130 μas and a proper motion precision of ~70 μas yr^{-1}, sufficient to both confirm that B and C are located at the same distance as KELT-21, and to detect the mutual orbital motion of the B–C and A–BC binaries. Although the companions are undetected in the *Gaia* DR1 source catalog, this is not unexpected given the large flux difference and the incompleteness of this catalog within 4″ of bright sources (Arenou et al. 2017). Given the low proper motion of KELT-21, it is likely that *Gaia* will confirm or refute the association of KELT-21 B and C with A before common proper motion confirmation is possible.

[51] http://stev.oapd.inaf.it/cgi-bin/trilegal_1.6
[52] http://model2016.obs-besancon.fr/
[53] https://irsa.ipac.caltech.edu/applications/DUST/
[54] https://www.cosmos.esa.int/web/gaia/science-performance

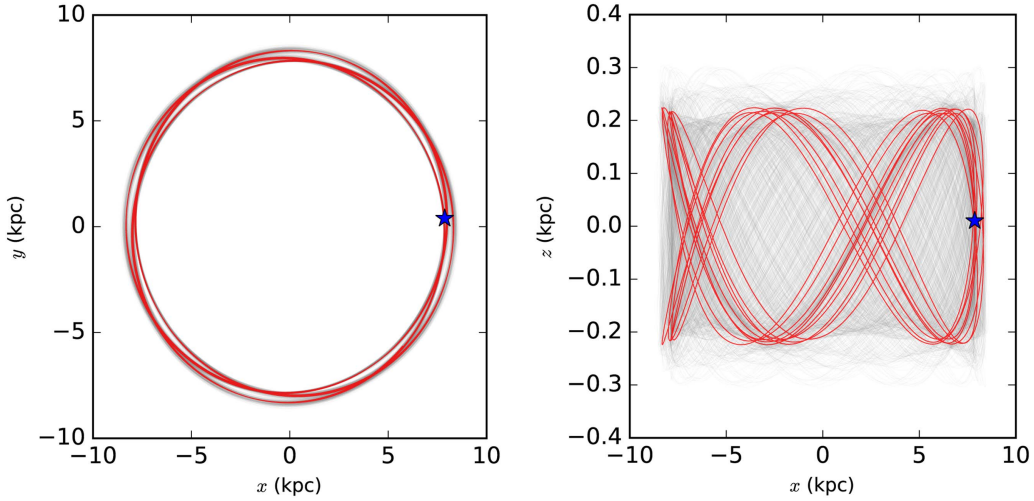

Figure 12. Galactic orbit of KELT-21, as computed with `galpy` from KELT-21's position, distance, and (U, V, W) space velocity, as viewed from the top in the x–y plane (left) and the side in the x–z plane (right). The red line shows the orbit computed over the next 2 Gyr using our computed parameters of KELT-21, while the gray lines show 50 realizations with values of (U, V, W) and distance randomly drawn from Gaussian distributions with the same mean and standard deviation as the measured value and uncertainty on each parameter. The blue star marks the current position of KELT-21. KELT-21 does not stray far from the solar circle or the Galactic plane, confirming its thin-disk kinematics.

5.2.3. Implications of the Companions

KELT-21b is likely one of the few known examples of a hot Jupiter in a hierarchical triple stellar system. Approximately 10% of field systems with AFGK primaries are stellar triple systems (Raghavan et al. 2010; De Rosa et al. 2014). Although it has been theoretically proposed that certain configurations of hierarchical triple systems should boost the efficiency of hot Jupiter formation (Hamers 2017), it is difficult to assess the occurrence rate of hot Jupiters in stellar triple systems due to observational biases against equal-mass triples and heterogeneous imaging observations across the full sample of known hot Jupiters; doing so is beyond the scope of this paper.

For binary companions to exoplanet host stars, we can evaluate whether the companion is capable of causing Kozai–Lidov oscillations by equating the Kozai–Lidov and general relativistic precession timescales (e.g., Ngo et al. 2016). Approximating KELT-21 BC as a single object with the sum of their masses, they would be capable of causing Kozai–Lidov oscillations of a giant planet with a semimajor axis of greater than $\sim$2.1 au if the A–BC mutual orbit is circular; this limit decreases as the eccentricity of this orbit increases (e.g., to $\sim$1.9 au for $e = 0.5$).

The dynamics of Kozai–Lidov oscillations due to a binary stellar companion, however, are more complicated than those due to a single companion (Fang et al. 2017; Hamers 2017). Hamers (2017) found in their simulations that in hierarchical triple systems with a structure similar to that of KELT-21 (i.e., a primary with a planet and a pair of binary companions, with $a_{B-C} \ll a_{A-BC}$, which they referred to as a "2+2" configuration), hot Jupiters tended to be formed only if $a_{B-C} \lesssim 10^2$ au, and 20 au $\lesssim a_{A-BC} \lesssim 10^3$ au. The period distribution of the resulting hot Jupiters in their models peaked around 3 days. Finally, Hamers (2017) found that Kozai–Lidov oscillations are enhanced if the Kozai–Lidov timescales for the planetary orbit, and the binary orbit of the companions, are similar; quantitatively, this occurs when $\mathcal{R}_{2+2} \sim (a_{B-C}/a_P)^{3/2}$ $[(M_* + M_P)/(M_B + M_C)]^{3/2} \sim \mathcal{O}(1)$. For the KELT-21 system, if the planet formed at 5 (15) au, the system would initially have had $\mathcal{R}_{2+2} \sim 150$ (30). Hamers (2017) found that hot Jupiters tend to form in systems with $0.01 \lesssim \mathcal{R}_{2+2} \lesssim 100$. The KELT-21 system is broadly consistent with all of these criteria, suggesting that it is plausible that the companions drove the migration of the planet by four-body Kozai–Lidov oscillations.

Nonetheless, the well-aligned orbit of KELT-21 is somewhat at odds with the Kozai–Lidov migration scenario. Hot Jupiters formed by this mechanism should frequently reside on highly inclined orbits (cf., Figure 9 of Hamers 2017). On the other hand, we found in Section 5.1 that KELT-21b has $\psi < 54\overset{\circ}{.}7$, which is reasonable given the distribution of ψ (there denoted θ_*) found by Hamers (2017).

We note in conclusion that given the many migration mechanisms that have been proposed to create hot Jupiters, it is always difficult or impossible to ascribe the formation of a specific system to a specific mechanism with any certainty. Instead, it is the distributions of parameters of a population (e.g., P, λ, etc.) that constrain the migration mechanisms. KELT-21b adds to the population of known hot Jupiters around hot stars, and thus will help to answer these questions statistically.

5.3. Metal Content and Galactic Context

The α-enhancement and relatively low metallicity found by our spectral analysis of KELT-21 (Section 3.2) are unusual for a relatively young ($\sim$1.6 Gyr) star. In order to better contextualize the low metallicity, we computed the Galactic orbit of KELT-21 using the `galpy` package[55] (Bovy 2015). Given our (U, V, W) values and using `galpy`'s "MWPotential2014" Galactic potential, we estimate that KELT-21's Galactic orbit has an apoapsis of at most $\sim$8.6 kpc and a periapsis of at minimum $\sim$7.7 kpc. This suggests that KELT-21 does not stray far from the solar circle, but its low metallicity could still be explained by invoking formation in the metal-poor outer Galaxy or Galactic bar followed by radial mixing due to the Milky Way's spiral arms (e.g., Sellwood & Binney 2002). See Figure 12 for a depiction of KELT-21's Galactic orbit. KELT-21 does not attain a height above the

[55] http://github.com/jobovy/galpy

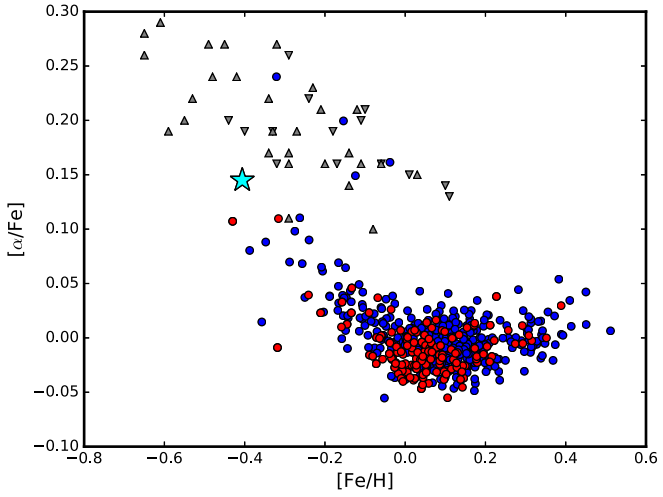

Figure 13. α-enhancement as a function of [Fe/H] for the APOKASC samples of 1.75 $M_{\odot} < M_{*} < 2.25$ $M_{\odot}$ giants (blue) and relatively young giants with kinematics similar to KELT-21 (red; see the text for details). KELT-21 is shown by the large cyan star. We also show the young α-rich stars found by Martig et al. (2015) and Chiappini et al. (2015) as downward- and upward-pointing gray triangles, respectively. Note that Martig et al. (2015) quote [Fe/M] and [α/M], not [Fe/H] and [α/Fe], and so the placement of these points on our plot should be considered approximate.

Galactic midplane of more than ∼300 pc, indicating that it is kinematically a member of the thin disk and substantiating our calculation that it has a high probability of being a member of the thin disk (Section 3.4). Its [α/Fe] value, however, is more similar to that of thick-disk than thin-disk stars at its [Fe/H] (cf. Bovy et al. 2016; Silva Aguirre et al. 2017), although it does lie in between the thin- and thick-disk chemical sequences.

In order to assess how unusual KELT-21 is for a relatively young field star, we utilized the APOKASC sample of stars with abundances, masses, and ages (M. H. Pinsonneault et al. 2018, in preparation; an update to the Pinsonneault et al. 2014 sample). These stars have asteroseismic parameters measured from *Kepler* photometry (Borucki et al. 2010), masses inferred from asteroseismic scaling relations (Kjeldsen & Bedding 1995) with theoretical corrections (Serenelli et al. 2017), and empirical calibrations to cluster data. They also have spectroscopic metallicities, temperatures, and abundances from Data Release 14 (Abolfathi et al. 2017) of the APOGEE-2 survey (Holtzman et al. 2015; Majewski et al. 2017) of the Sloan Digital Sky Survey IV (Blanton et al. 2017) on the Sloan Digital Sky Survey telescope (Gunn et al. 2006). For our comparison, we assessed the values of [Fe/H] and [α/Fe] for two subsamples: giants with masses of 1.75 $M_{\odot} < M_{*} < 2.25$ $M_{\odot}$, which should have formed at around the same time as KELT-21, and stars with ages of less than 1.7 Gyr and *Gaia* parallaxes from which we could compute Galactic kinematics, again using `galpy` (Bovy 2015). For the latter sample, we selected stars with Galactic periapses >6.6 kpc and apoapses <10.0 kpc in order to produce a sample with similar kinematics to KELT-21. For both samples, we excluded stars with [C/N] > −0.4 in order to exclude stars that are likely merger products or have experienced significant mass gain due to binary interactions, and are therefore likely older than would be assumed given their other properties (cf., Izzard et al. 2018). We show the resulting [Fe/H] and [α/Fe] values in Figure 13. It is apparent that KELT-21's [Fe/H] is at the lower end of these distributions, but it is not a dramatic outlier. We thus conclude that while KELT-21's low metallicity is unusual for a relatively young star that is kinematically part of the thin disk, it is not inexplicably so.

KELT-21's abundance pattern and relatively young age are qualitatively similar to those of the class of young, α-rich giants found through the combination of *Kepler*/*CoRoT* asteroseismology and APOGEE spectra by Martig et al. (2015) and Chiappini et al. (2015), although KELT-21 falls at the edge of the distribution of such stars (Figure 13). KELT-21 could be such a star observed while it is still on the main sequence. Such stars found by Chiappini et al. (2015) were primarily in the inner Galactic disk, and they invoked formation at the end of the Galactic bar; although this is inconsistent with KELT-21's current circular orbit and location near the solar circle, as mentioned earlier it could still have formed in the inner Galaxy and experienced radial mixing to move it to its current location, although this would have needed to be rapid in order to move the star several kiloparsecs within the 1.6 Gyr since it formed. The planet orbiting KELT-21 also seems to be at odds with the other proposed explanation for young α-rich stars, namely, that they are blue stragglers formed from stellar mergers (Jofré et al. 2016; Yong et al. 2016). Such a collision would have destroyed any short-period planet already around one of the stars; KELT-21b would have needed to either form from material thrown off in the collision, or have survived the collision at a larger semimajor axis and only migrated *after* the collision. Young α-rich stars also tend to be kinematically members of the thick disk, while KELT-21 is not, and so the association of KELT-21 with this class is not clear.

KELT-21's low metallicity is also unusual for a hot Jupiter host. Giant planets are much more common around more metal-rich stars; this is the well-known planet–metallicity correlation (e.g., Fischer & Valenti 2005). Only a handful of hot Jupiters are known to orbit stars more metal poor than KELT-21, the current record holder being WASP-98, with [Fe/H] = −0.60 (Hellier et al. 2014). KELT-21b is thus useful for probing the properties of giant planets at low metallicity. Additionally, planet-host stars at low metallicity tend to be significantly α-enhanced (e.g., Adibekyan et al. 2012). It is thought that this is because stars with higher [α/Fe] have more metals available to form solids (and therefore planets) at fixed [Fe/H]. KELT-21's α-enhancement is in between the values typical for the thick- and thin-disk populations, which is not inconsistent with this trend.

5.4. Prospects for Characterization

Although KELT-21 is, at $V = 10.5$, one of the fainter transiting planet hosts found by KELT, it is nonetheless brighter than many transiting planet hosts (cf., the *Kepler* sample), and so prospects for further characterization are good. In Figure 14, we show KELT-21 in the context of the population of known transiting planets, in terms of host star optical magnitude and $T_{\rm eff}$. Only a few stars hotter than KELT-21 host transiting hot Jupiters, and due to its relatively long-period orbit compared to these planets (3.6 days), KELT-21b is relatively cool (zero-albedo equilibrium temperature of $T_{\rm eq} = 2051$ K), potentially offering interesting prospects for atmospheric characterization via transmission spectroscopy.

KELT-21 is also relatively bright in the infrared ($J = 10.15$, $K_S = 10.09$; Table 1), suggesting that KELT-21b may also be a

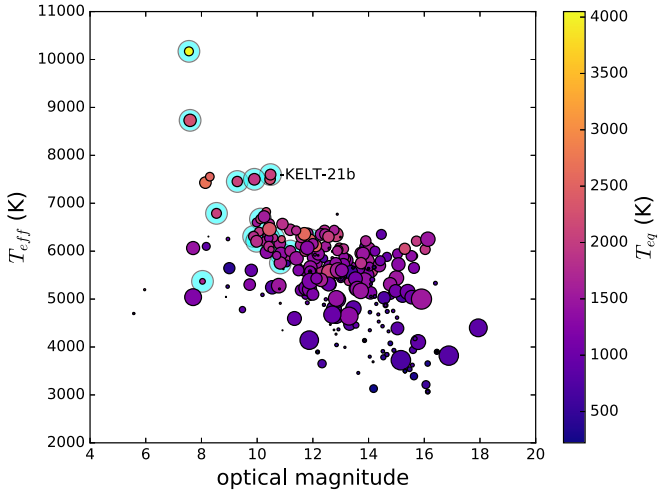

Figure 14. KELT-21 in context with other known planets for the purpose of atmospheric investigations. The symbol color corresponds to the planetary zero-albedo equilibrium temperature, while the symbol size is proportional to the transit depth $(R_P/R_*)^2$. Planets discovered by KELT are marked with large cyan circles. KELT-21 is hotter and brighter than most transiting exoplanet hosts, and prospects for observations to characterize the atmosphere are good. The optical magnitude on the horizontal axis is the *Kp* magnitude for *Kepler* planets and the *V* magnitude for most other objects. We show known transiting planets taken from the NASA Exoplanet Archive (https://exoplanetarchive.ipac.caltech.edu/), plus KELT-19Ab (Siverd et al. 2018), KELT-20b/MASCARA-2b (Lund et al. 2017; Talens et al. 2017b), and MASCARA-1b (Talens et al. 2017a). The location of KELT-21b is marked.

good target for secondary eclipse observations in the infrared. This will help to constrain the atmospheric properties of KELT-21b, either alone or in concert with transmission spectroscopy during the transit.

Due to the high $v \sin I_*$ of KELT-21, we have been unable to measure the mass of KELT-21b, only set a 3σ upper limit of $M_P < 3.91\ M_J$. Future observations might be able to measure the mass; however, the rapid rotation of KELT-21 will make this very difficult. Another possible avenue to measure the mass and probe the atmosphere of KELT-21b is through the detection of the orbital phase curve (e.g., Shporer et al. 2011). We estimate that, in the *TESS* bandpass, KELT-21 should have an orbital phase curve amplitude of ∼65 ppm. KELT-21 (TIC 203189770) has a *TESS* bandpass magnitude of 10.33, which should result in a per-point photometric precision of ∼240 ppm (using the noise–*T* magnitude relationship presented in Stassun et al. 2017), and will be on *TESS* silicon for up to 54.8 days in *TESS* Year 2 (as KELT-21 is in the northern ecliptic hemisphere). This precision and duration of data, folded over the orbital period of the planet and binned, result in a precision of ∼60 ppm, suggesting that the phase curve of KELT-21b should be detectable by *TESS*. Due to the high equilibrium temperature, the *TESS* bandpass phase curve should be dominated by thermal emission from the planet (amplitude ∼35 ppm), which would be even more prominent in the infrared; this may also be detectable with *Spitzer*.

6. Summary and Conclusion

We have presented the discovery of KELT-21b, a hot Jupiter on a 3.6 day orbit transiting the rapidly rotating A8V star HD 332124. With $v \sin I_* = 146\ \mathrm{km\ s^{-1}}$, KELT-21 is the most rapidly rotating star to host a confirmed transiting planet to date, and KELT-21b is one of only a handful of known transiting planets around an A star. Its host star is also relatively bright, suggesting good prospects for follow-up observations to further characterize the planet.

Our high-resolution imaging observations revealed the presence of a close pair of faint stars at a separation of 1.″2 from the planet-host star. Although we cannot confirm using our current data whether they are physically associated with the KELT-21 system, we have argued statistically that they are unlikely to be background sources. If they are indeed physically associated with KELT-21, KELT-21 B and C are a pair of mid-M dwarfs with a mutual separation of ∼20 au, lying ∼500 au from KELT-21. They occupy the part of parameter space where they could have caused the migration of KELT-21b through the Kozai–Lidov mechanism (e.g., Hamers 2017), although the well-aligned orbit of KELT-21b is not entirely consistent with such an origin.

Unusually for a star of its relatively high mass and thus relatively young age, KELT-21 appears to have a somewhat low metallicity ($[\mathrm{Fe/H}] = -0.405^{+0.032}_{-0.033}$) and an α-enhancement ($[\alpha/\mathrm{Fe}] = 0.145 \pm 0.053$). Although this metallicity is unusual for a relatively young (∼1.6 Gyr) star with thin-disk kinematics, it is not inexplicably so, and the $[\alpha/\mathrm{Fe}]$ is more typical of thick-disk stars at this [Fe/H]. KELT-21b is also among the lowest-metallicity stars known to host a hot Jupiter and is thus particularly interesting in the context of planet formation theory.

We thank Jennifer Johnson, Marc Pinsonneault, and Dennis Stello for useful discussions on the Galactic context of KELT-21 and the analysis using the APOKASC catalog.

Work performed by J.E.R. was supported by the Harvard Future Faculty Leaders Postdoctoral fellowship. Work by G.Z. is provided by NASA through Hubble Fellowship grant *HST*-HF2-51402.001-A awarded by the Space Telescope Science Institute, which is operated by the Association of Universities for Research in Astronomy, Inc., for NASA, under contract NAS 5-26555. Work performed by P.A.C. was supported by NASA grant NNX13AI46G. K.P. acknowledges support from NASA grant NNX13AQ62G. B.S.G. and D.J.S. were partially supported by NSF CAREER Grant AST-1056524. A.S. is partially supported by grant ESP2015-66134-R. Funding for the Stellar Astrophysics Centre is provided by The Danish National Research Foundation (grant agreement No. DNRF106). V.S.A. acknowledges support from VILLUM FONDEN (research grant 10118).

This project makes use of data from the KELT survey, including support from The Ohio State University, Vanderbilt University, and Lehigh University, along with the KELT follow-up collaboration. The LBT is an international collaboration among institutions in the United States, Italy, and Germany. The LBT Corporation partners are The Ohio State University; LBT Beteiligungsgesellschaft, Germany, representing the Max Planck Society, the Astrophysical Institute Potsdam, and Heidelberg University; The University of Arizona on behalf of the Arizona university system; Istituto Nazionale di Astrofisica, Italy; and The Research Corporation, on behalf of The University of Notre Dame, University of Minnesota, and University of Virginia. This paper includes data taken at The McDonald Observatory of The University of Texas at Austin. Some of the data presented herein were obtained at the W. M. Keck Observatory, which is operated as a scientific partnership among the California Institute of

Technology, the University of California and the National Aeronautics and Space Administration. The Observatory was made possible by the generous financial support of the W. M. Keck Foundation. The authors wish to recognize and acknowledge the very significant cultural role and reverence that the summit of Maunakea has always had within the indigenous Hawaiian community. We are most fortunate to have the opportunity to conduct observations from this mountain. This work has made use of NASA's Astrophysics Data System, the Extrasolar Planet Encyclopedia at exoplanet.eu, the SIMBAD database operated at CDS, Strasbourg, France, and the VizieR catalog access tool, CDS, Strasbourg, France. We also used data products from the Wide-field Infrared Survey Explorer, which is a joint project of the University of California, Los Angeles, and the Jet Propulsion Laboratory/California Institute of Technology, funded by the National Aeronautics and Space Administration; the Two Micron All-Sky Survey, which is a joint project of the University of Massachusetts and the Infrared Processing and Analysis Center/California Institute of Technology, funded by the National Aeronautics and Space Administration and the National Science Foundation; and the European Space Agency (ESA) mission *Gaia* (http://www.cosmos.esa.int/gaia), processed by the *Gaia* Data Processing and Analysis Consortium (DPAC; http://www.cosmos.esa.int/web/gaia/dpac/consortium). Funding for the DPAC has been provided by national institutions, in particular the institutions participating in the *Gaia* Multilateral Agreement.

Facilities: KELT, LBT (PEPSI), FLWO (TRES), Smith (TS23), Keck (NIRC2).

Software: Python, IDL, IRAF, TAPIR (Jensen 2013), AstroImageJ (Collins & Kielkopf 2013), SDS4PEPSI (Strassmeier et al. 2017), EXOFAST (Eastman et al. 2013), POET (Penev et al. 2014), TRILEGAL (Girardi et al. 2005), Besançon (Robin et al. 2003), isochrones (Morton 2015), galpy (Bovy 2015).

ORCID iDs

Marshall C. Johnson https://orcid.org/0000-0002-5099-8185
Joseph E. Rodriguez https://orcid.org/0000-0001-8812-0565
George Zhou https://orcid.org/0000-0002-4891-3517
Justin R. Crepp https://orcid.org/0000-0003-0800-0593
Kaloyan Penev https://orcid.org/0000-0003-4464-1371
Keivan G. Stassun https://orcid.org/0000-0002-3481-9052
B. Scott Gaudi https://orcid.org/0000-0003-0395-9869
Knicole D. Colón https://orcid.org/0000-0001-8020-7121
Daniel J. Stevens https://orcid.org/0000-0002-5951-8328
Karen A. Collins https://orcid.org/0000-0001-6588-9574
John F. Kielkopf https://orcid.org/0000-0003-0497-2651
Phillip A. Reed https://orcid.org/0000-0002-5005-1215
Valerio Bozza https://orcid.org/0000-0003-4590-0136
Sebastiano Calchi Novati https://orcid.org/0000-0002-7669-1069
Giuseppe D'Ago https://orcid.org/0000-0001-9697-7331
David W. Latham https://orcid.org/0000-0001-9911-7388
Allyson Bieryla https://orcid.org/0000-0001-6637-5401
William D. Cochran https://orcid.org/0000-0001-9662-3496
Michael Endl https://orcid.org/0000-0002-7714-6310
Jamie Tayar https://orcid.org/0000-0002-4818-7885
Victor Silva Aguirre https://orcid.org/0000-0002-6137-903X
Michael D. Joner https://orcid.org/0000-0003-0634-8449
Eric G. Hintz https://orcid.org/0000-0002-9867-7938
Kim K. McLeod https://orcid.org/0000-0001-9504-1486
Eric L. N. Jensen https://orcid.org/0000-0002-4625-7333
Hannah Jang-Condell https://orcid.org/0000-0002-7639-1322
Thomas G. Beatty https://orcid.org/0000-0002-9539-4203
Jason Eastman https://orcid.org/0000-0003-3773-5142
David James https://orcid.org/0000-0001-5160-4486
Rudolf B. Kuhn https://orcid.org/0000-0002-4236-9020
Jonathan Labadie-Bartz https://orcid.org/0000-0002-2919-6786
Michael B. Lund https://orcid.org/0000-0003-2527-1598
Joshua Pepper https://orcid.org/0000-0002-3827-8417
Robert J. Siverd https://orcid.org/0000-0001-5016-3359
David H. Cohen https://orcid.org/0000-0003-2995-4767
Benjamin J. Fulton https://orcid.org/0000-0003-3504-5316
Matthew T. Penny https://orcid.org/0000-0001-7506-5640
Christopher Stockdale https://orcid.org/0000-0003-2163-1437
Thiam-Guan Tan https://orcid.org/0000-0001-5603-6895
Steven Villanueva, Jr. https://orcid.org/0000-0001-6213-8804

References

Abolfathi, B., Aguado, D. S., Aguilar, G., et al. 2017, arXiv:1707.09322
Adibekyan, V. Z., Santos, N. C., Sousa, S. G., et al. 2012, A&A, 543, A89
Arenou, F., Luri, X., Babusiaux, C., et al. 2017, A&A, 599, A50
Bechter, E. B., Crepp, J. R., Ngo, H., et al. 2014, ApJ, 788, 2
Bensby, T., Feltzing, S., & Lundström, I. 2003, A&A, 410, 527
Bieryla, A., Collins, K. A., Beatty, T. G., et al. 2015, AJ, 150, 12
Blanton, M. R., Bershady, M. A., Abolfathi, B., et al. 2017, AJ, 154, 28
Borucki, W. J., Koch, D., Basri, G., et al. 2010, Sci, 327, 977
Bovy, J. 2015, ApJS, 216, 29
Bovy, J., Rix, H.-W., Schlafly, E. F., et al. 2016, ApJ, 823, 30
Buchhave, L. A., Bakos, G. Á, Hartman, J. D., et al. 2010, ApJ, 720, 1118
Carter, J. A., & Winn, J. N. 2009, ApJ, 704, 51
Castelli, F., & Kurucz, R. L. 2004, arXiv:astro-ph/0405087
Chiappini, C., Anders, F., Rodrigues, T. S., et al. 2015, A&A, 576, L12
Coşkunoğlu, B., Ak, S., Bilir, S., et al. 2011, MNRAS, 412, 1237
Collier Cameron, A., Guenther, E., Smalley, B., et al. 2010, MNRAS, 407, 507
Collins, K. A., & Kielkopf, J. 2013, AstroImageJ: ImageJ for Astronomy, Astrophysics Source Code Library, ascl:1309.001
Collins, K. A., Eastman, J. D., Beatty, T. G., et al. 2014, AJ, 147, 39
Collins, K. A., Kielkopf, J. F., Stassun, K. G., & Hessman, F. V. 2017, AJ, 153, 77
Crepp, J. R., Johnson, J. A., Howard, A. W., et al. 2012, ApJ, 761, 39
Crouzet, N., McCullough, P. R., Long, D., et al. 2017, AJ, 153, 94
Cutri, R. M., Skrutskie, M. F., van Dyk, S., et al. 2003, yCat, 2246, 0
Cutri, R. M., et al. 2014, yCat, 2328, 0
Dawson, R. I., & Murray-Clay, R. A. 2013, ApJL, 767, L24
De Rosa, R. J., Patience, J., Wilson, P. A., et al. 2014, MNRAS, 437, 1216
Demarque, P., Woo, J.-H., Kim, Y.-C., & Yi, S. K. 2004, ApJS, 155, 667
Donati, J.-F., Semel, M., Carter, B. D., Rees, D. E., & Collier Cameron, A. 1997, MNRAS, 291, 658
Eastman, J., Gaudi, B. S., & Agol, E. 2013, PASP, 125, 83
Eastman, J., Siverd, R., & Gaudi, B. S. 2010, PASP, 122, 935
Eastman, J. D., Beatty, T. G., Siverd, R. J., et al. 2016, AJ, 151, 45
Evans, D. F., Southworth, J., Maxted, P. F. L., et al. 2016, A&A, 589, A58
Fabrycky, D., & Tremaine, S. 2007, ApJ, 669, 1298
Fang, X., Thompson, T. A., & Hirata, C. M. 2017, arXiv:1709.08682
Fűrész, G. 2008, PhD thesis, Univ. Szeged
Fischer, D. A., & Valenti, J. 2005, ApJ, 622, 1102
Fulton, B. J., Collins, K. A., Gaudi, B. S., et al. 2015, ApJ, 810, 30
Gaia Collaboration, Brown, A. G. A., Vallenari, A., et al. 2016, A&A, 595, A2
Gandolfi, D., Collier Cameron, A., Endl, M., et al. 2012, A&A, 543, L5
Gandolfi, D., Hébrard, G., Alonso, R., et al. 2010, A&A, 524, A55
Gaudi, B. S., Stassun, K. G., Collins, K. A., et al. 2017, Natur, 546, 514
Girardi, L., Groenewegen, M. A. T., Hatziminaoglou, E., & da Costa, L. 2005, A&A, 436, 895
Green, G. M., Schlafly, E. F., Finkbeiner, D. P., et al. 2015, ApJ, 810, 25
Gunn, J. E., Siegmund, W. A., Mannery, E. J., et al. 2006, AJ, 131, 2332

Hamers, A. S. 2017, MNRAS, 466, 4107
Hartman, J. D., Bakos, G. Á, Buchhave, L. A., et al. 2015, AJ, 150, 197
Heacox, W. D., & Gathright, J. 1994, AJ, 108, 1101
Hellier, C., Anderson, D. R., Cameron, A. C., et al. 2014, MNRAS, 440, 1982
Høg, E., Fabricius, C., Makarov, V. V., et al. 2000, A&A, 355, L27
Holtzman, J. A., Shetrone, M., Johnson, J. A., et al. 2015, AJ, 150, 148
Ilyin, I. V. 2000, PhD thesis, Univ. Oulu Finland
Iorio, L. 2011, Ap&SS, 331, 485
Izzard, R. G., Preece, H., Jofre, P., et al. 2018, MNRAS, 473, 2984
Jensen, E. 2013, Tapir: A Web Interface for Transit/Eclipse Observability, Astrophysics Source Code Library, ascl:1306.007
Jofré, P., Jorissen, A., Van Eck, S., et al. 2016, A&A, 595, A60
Johnson, D. R. H., & Soderblom, D. R. 1987, AJ, 93, 864
Johnson, J. A., Clanton, C., Howard, A. W., et al. 2011, ApJS, 197, 26
Johnson, J. A., Morton, T. D., & Wright, J. T. 2013, ApJ, 763, 53
Johnson, M. C., Cochran, W. D., Addison, B. C., Tinney, C. G., & Wright, D. J. 2017, AJ, 154, 137
Johnson, M. C., Cochran, W. D., Albrecht, S., et al. 2014, ApJ, 790, 30
Johnson, M. C., Cochran, W. D., Collier Cameron, A., & Bayliss, D. 2015, ApJL, 810, L23
Jordi, C., Gebran, M., Carrasco, J. M., et al. 2010, A&A, 523, A48
Kjeldsen, H., & Bedding, T. R. 1995, A&A, 293, 87
Kraft, R. P. 1967, ApJ, 150, 551
Kurucz, R. L. 1979, ApJS, 40, 1
Kurucz, R. L. 1992, in IAU Symp. 149, The Stellar Populations of Galaxies, ed. B. Barbuy & A. Renzini (Dordrecht: Kluwer), 225
Lagrange, A.-M., Bonnefoy, M., Chauvin, G., et al. 2010, Sci, 329, 57
Lin, D. N. C., Bodenheimer, P., & Richardson, D. C. 1996, Natur, 380, 606
Lloyd, J. P. 2011, ApJL, 739, L49
Lund, M. B., Rodriguez, J. E., Zhou, G., et al. 2017, AJ, 154, 194
Majewski, S. R., Schiavon, R. P., Frinchaboy, P. M., et al. 2017, AJ, 154, 94
Marois, C., Macintosh, B., Barman, T., et al. 2008, Sci, 322, 1348
Marois, C., Zuckerman, B., Konopacky, Q. M., Macintosh, B., & Barman, T. 2010, Natur, 468, 1080
Marshall, D. J., Robin, A. C., Reylé, C., Schultheis, M., & Picaud, S. 2006, A&A, 453, 635
Martig, M., Rix, H.-W., Silva Aguirre, V., et al. 2015, MNRAS, 451, 2230
McLaughlin, D. B. 1924, ApJ, 60, 22
McLeod, K. K., Rodriguez, J. E., Oelkers, R. J., et al. 2017, AJ, 153, 263
Morton, T. D. 2015, isochrones: Stellar model grid package Astrophysics Source Code Library, ascl:1503.010
Naoz, S., Farr, W. M., & Rasio, F. A. 2012, ApJL, 754, L36
Ngo, H., Knutson, H. A., Hinkley, S., et al. 2016, ApJ, 827, 8
Oberst, T. E., Rodriguez, J. E., Colón, K. D., et al. 2017, AJ, 153, 97
Pecaut, M. J., & Mamajek, E. E. 2013, ApJS, 208, 9
Penev, K., Zhang, M., & Jackson, B. 2014, PASP, 126, 553
Pepper, J., Gould, A., & Depoy, D. L. 2003, AcA, 53, 213
Pepper, J., Kuhn, R. B., Siverd, R., James, D., & Stassun, K. 2012, PASP, 124, 230
Pepper, J., Pogge, R. W., DePoy, D. L., et al. 2007, PASP, 119, 923
Pepper, J., Rodriguez, J. E., Collins, K. A., et al. 2017, AJ, 153, 215
Pepper, J., Siverd, R. J., Beatty, T. G., et al. 2013, ApJ, 773, 64
Pinsonneault, M. H., Elsworth, Y., Epstein, C., et al. 2014, ApJS, 215, 19
Quinn, S. N., Bakos, G. Á, Hartman, J., et al. 2012, ApJ, 745, 80
Raghavan, D., McAlister, H. A., Henry, T. J., et al. 2010, ApJS, 190, 1
Reffert, S., Bergmann, C., Quirrenbach, A., Trifonov, T., & Künstler, A. 2015, A&A, 574, A116
Rix, H.-W., Ting, Y.-S., Conroy, C., & Hogg, D. W. 2016, ApJL, 826, L25
Robin, A. C., Reylé, C., Derrière, S., & Picaud, S. 2003, A&A, 409, 523
Rossiter, R. A. 1924, ApJ, 60, 15
Royer, F., Zorec, J., & Gómez, A. E. 2007, A&A, 463, 671
Ryabchikova, T., Piskunov, N., Kurucz, R. L., et al. 2015, PhyS, 90, 054005
Santerne, A., Moutou, C., Barros, S. C. C., et al. 2012, A&A, 544, L12
Schlafly, E. F., & Finkbeiner, D. P. 2011, ApJ, 737, 103
Schlaufman, K. C. 2010, ApJ, 719, 602
Schlaufman, K. C., & Winn, J. N. 2013, ApJ, 772, 143
Schlegel, D. J., Finkbeiner, D. P., & Davis, M. 1998, ApJ, 500, 525
Sellwood, J. A., & Binney, J. J. 2002, MNRAS, 336, 785
Serenelli, A., Johnson, J., Huber, D., et al. 2017, ApJS, 233, 23
Shporer, A., Jenkins, J. M., Rowe, J. F., et al. 2011, AJ, 142, 195
Silva Aguirre, V., Bojsen-Hansen, M., Slumstrup, D., et al. 2017, arXiv:1710.09847
Siverd, R. J., Beatty, T. G., Pepper, J., et al. 2012, ApJ, 761, 123
Siverd, R. J., Collins, K. A., Zhou, G., et al. 2018, AJ, 155, 35
Smith, A. J., Loveday, J., & Cross, N. J. G. 2009, MNRAS, 397, 868
Stassun, K. G., Oelkers, R. J., Pepper, J., et al. 2017, arXiv:1706.00495
Stassun, K. G., & Torres, G. 2016, ApJL, 831, L6
Stello, D., Huber, D., Grundahl, F., et al. 2017, MNRAS, 472, 4110
Stevens, D. J., Collins, K. A., Gaudi, B. S., et al. 2017, AJ, 153, 178
Strassmeier, K. G., Ilyin, I., Järvinen, A., et al. 2015, AN, 336, 324
Strassmeier, K. G., Ilyin, I., & Steffen, M. 2017, A&A, submitted, arXiv:1712.06960
Szabó, G. M., Szabó, R., Benkő, J. M., et al. 2011, ApJL, 736, L4
Talens, G. J. J., Albrecht, S., Spronck, J. F. P., et al. 2017a, A&A, 606, A73
Talens, G. J. J., Justesen, A. B., Albrecht, S., et al. 2017b, arXiv:1707.01500
Temple, L. Y., Hellier, C., Albrow, M. D., et al. 2017, MNRAS, 471, 2743
Ting, Y.-S., Conroy, C., & Rix, H.-W. 2016, ApJ, 826, 83
Torres, G., Andersen, J., & Giménez, A. 2010, A&Ar, 18, 67
Triaud, A. H. M. J., Collier Cameron, A., Queloz, D., et al. 2010, A&A, 524, A25
Tull, R. G., MacQueen, P. J., Sneden, C., & Lambert, D. L. 1995, PASP, 107, 251
Winn, J. N., Fabrycky, D., Albrecht, S., & Johnson, J. A. 2010, ApJL, 718, L145
Winn, J. N., Petigura, E. A., Morton, T. D., et al. 2017, AJ, 154, 270
Yong, D., Casagrande, L., Venn, K. A., et al. 2016, MNRAS, 459, 487
Zhou, G., Latham, D. W., Bieryla, A., et al. 2016a, MNRAS, 460, 3376
Zhou, G., Rodriguez, J. E., Collins, K. A., et al. 2016b, AJ, 152, 136